A HYBRID MODEL TO ANALYZE STRESS DISTRIBUTIONS AT THE TOOL AND WORKPIECE INTERFACE DURING DRILLING OF THICK CFRP LAMINATES

A THESIS SUBMITTED TO

THE GRADUATE SCHOOL OF ENGINEERING AND SCIENCE

OF BILKENT UNIVERSITY

IN PARTIAL FULFILLMENT OF THE REQUIREMENTS FOR

THE DEGREE OF

MASTER OF SCIENCE

IN

MECHANICAL ENGINEERING

By

Fahim Shariar

August 2024

A HYBRID MODEL TO ANALYZE STRESS DISTRIBUTIONS AT THE TOOL AND WORKPIECE INTERFACE DURING DRILLING OF THICK CFRP LAMINATES

By Fahim Shariar

August 2024

We certify that we have read this thesis and that in our opinion it is fully adequate, in scope and in quality, as a thesis for the degree of Master of Science.

Yiğit Karpat(Advisor)

Orkun Özşahin

İlker Temizer

Approved for the Graduate School of Engineering and Science:

Orhan Arıkan
Director of the Graduate School

ABSTRACT

A HYBRID MODEL TO ANALYZE STRESS DISTRIBUTIONS AT THE TOOL AND WORKPIECE INTERFACE DURING DRILLING OF THICK CFRP LAMINATES

Fahim Shariar
M.S. in Mechanical Engineering
Advisor: Yiğit Karpat
August 2024

Drilling is employed as a machining method to meet the demands for producing functional CFRP structures without compromising their unique and desirable material properties. Because of its temperature-dependent properties and drill-induced damages, drilling CFRP remains an ambitious task. This study proposes an analytical drilling model coupled with a finite element-based thermal model to predict the characteristic time point-based thrust force and torque generated during the drilling operation. A better understanding of pressure and tangential stress distribution along the drilling cutting edge is necessary to select process parameters better. The drill margin region, which directly affects the hole wall quality, has also been included in the analysis. Drilling experiments were conducted to measure thrust force, torque, and temperature for five different configurations of feeds and spindle speeds. The workpiece FE model utilizes a Gaussian distributed ring-type heat flux, and the tool uses characteristic time point-based step functions as heat fluxes to emulate the drill's progress through the CFRP laminate. The finite element-based thermal models have been considered to evaluate the heat partition during the drilling operation and estimate the subsequent temperature profiles on the drill tip and hole wall surface, respectively. The hybrid analytical and computational model has been used to analyze the variation of peak pressure and tangential stress distributions on the tip of the drill as well as the thermomechanical response of CFRP based on experimental measurements of thrust force, torque, and temperature and investigation of the condition of the holes for various drilling configurations.

Keywords: Drilling, Mechanical stress distributions, Polycrystalline diamond (PCD), Fiber reinforced polymer (FRP), Heat Partition.

ÖZET

KALIN CFRP LAMİNATLARIN DELİNMESİ ESNASINDA TAKIM VE PARÇA ARAYÜZÜNDEKİ GERİLİM DAĞILIMLARININ ANALİZ EDİLEBİLMESİ İÇİN HİBRİT BİR MODEL

Fahim Shariar
Makine Mühendisliği, Yüksek Lisans
Tez Danışmanı: Yiğit Karpat
Ağustos 2024

Delme, benzersiz ve istenen malzeme özelliklerinden ödün vermeden fonksiyonel CFRP yapılarının üretilmesine yönelik talepleri karşılamak için bir işleme yöntemi olarak kullanılır. Sıcaklığa bağlı özellikleri ve matkaptan kaynaklanan hasarlar nedeniyle CFRP'yi delmek iddialı bir görev olmaya devam ediyor. Bu çalışma, sondaj işlemi sırasında üretilen karakteristik zaman noktası bazlı itme kuvveti ve torku tahmin etmek için sonlu eleman bazlı termal modelle birleştirilmiş analitik bir sondaj modeli önermektedir. Proses parametrelerinin daha iyi seçilmesi için sondaj kesme kenarı boyunca basınç ve teğetsel gerilim dağılımının daha iyi anlaşılması gerekir. Delik duvar kalitesini doğrudan etkileyen matkap marjı bölgesi de analize dahil edilmiştir. Beş farklı ilerleme ve iş mili hızı konfigürasyonu için itme kuvvetini, torku ve sıcaklığı ölçmek amacıyla delme deneyleri yapıldı. İş parçası FE modeli, Gaussian dağıtılmış halka tipi ısı akısı kullanır ve alet, matkabın CFRP laminat boyunca ilerleyişini taklit etmek için ısı akısı olarak karakteristik zaman noktası tabanlı adım fonksiyonlarını kullanır. Sonlu eleman tabanlı termal modeller, delme işlemi sırasındaki ısı dağılımını değerlendirmek ve sırasıyla matkap ucu ve delik duvarı yüzeyindeki sonraki sıcaklık profillerini tahmin etmek için dikkate alınmıştır. Hibrit analitik ve hesaplamalı model, matkabın ucundaki tepe basınç ve teğetsel gerilim dağılımlarının değişimini analiz etmek ve ayrıca itme kuvveti, tork ve sıcaklığın deneysel ölçümlerine ve malzemenin incelenmesine dayalı CFRP'nin termomekanik tepkisini analiz etmek için kullanılmıştır. Çeşitli delme konfigürasyonları için deliklerin durumu.

Anahtar sözcükler: Delme, Mekanik gerilim dağılımları, Polikristalin elmas (PCD), Fiber takviyeli polimer (FRP), Isı Bölme.

Acknowledgement

I would like to begin by thanking my advisor Dr. Yiğit Karpat, whom I had the privilege of working with for the past 3 years. His unwavering support has been instrumental in my journey in the Precision Manufacturing Research Group. I especially appreciate the time he took to sincerely discuss and offer advice for all the difficulties and queries I have faced in the process. As an international student pursuing study abroad, it wasn't easy to get accustomed to a different country and culture immediately. I am genuinely grateful to him for giving me ample time to get accustomed to the academic culture at Bilkent University and find my own pace. I admire his motivation to pursue research and aspire to be as enthusiastic as him.

I want to thank my thesis committee, Asst. Prof. Dr. Orkun Özşahin for his valuable insights and ideas and also Prof. Dr. İlker Temizer for his discussions as well as his contributions during my graduate studies. I also am immensely grateful to them for taking precious time from their schedule and agreeing to be a part of my thesis jury.

I am thankful to Assc. Prof. Umut Karaguzel of Yıldız Technical University and Prof. Mustafa Bakkal of Istanbul Technical University for their contributions during the experimental work of this study.

I am forever grateful to my parents for providing me the opportunity to come this far in my journey. Their continuous support and diligence have been and will always be instrumental in my life. I especially want to thank my mother for patiently waiting for me for the last 3 years as I have continued my studies here. Her prayer, support, and love have been the shining light during the tough times. I am thankful to my younger brother Abir for all the time he has spent with me over the phone accompanying me even though he is also busy pursuing his studies.

I am indebted to Sayedus Salehin for his guidance, discussions, and assistance

throughout this journey as a mentor as well as a deskmate. I am grateful to Humayun Ahmed for all the interesting discussions and problem-solving sessions which were crucial in enhancing my understanding of various subject matters. In addition, I want to thank Ozgur Can Gumus, Emirhan inanç, Aykut Bakan, and Md. Fahmid Matin Bhuyian for their insights and knowledge.

Lastly, I want to thank the Bangladeshi community at Bilkent for their hospitality, support, and precious time which has helped me find another home outside my home country. I had the privilege of spending quality and blissful time here thanks to each one of these people.

Contents

List of Figures

List of Tables

Chapter 1

Introduction

1.1 Carbon Fiber Reinforced Polymer (CFRP)

After the accidental discovery of carbon fibers in the 1950s, the desire to enable their use in practical settings led to their subsequent involvement in polymer-based matrices, which laid the groundwork for the development of carbon fiber-reinforced polymers. CFRPs rose to prominence due to their unique and lucrative material properties that made way for them to be used in various sectors such as aerospace, automotive, sports, defense, etc. [1, 2, 3, 4]. The aerospace industry has been searching for ways to reduce their fuel consumption to make the services more efficient for their customers. However, due to the use of traditional metals like titanium, the aircraft were heavier and thus required more fuel to keep them flying. Because CFRP's tensile strength is 14 times higher than titanium, weighting only half due to lower density was an alternative that revolutionized the aerospace industry [5]. Impressive fatigue and corrosion resistance made it popular in the automotive and marine industries as components built from it could endure higher amounts of stress cycles subjected to loading [6]. When using CFRP for structural parts, the most common methods of assembly connection between CFRP structural parts and other parts are through bolts [7]. The holes

required for bolt connections are acquired through machining operations, primarily dry drilling. Since a large number of holes are required for large structural assembly, the quality of the holes becomes a key factor during production. Low thermal conductivity of CFRP means that more heat can be accumulated at the cutting interface which can damage both the material and the tool. Due to the complex structure of the composite, its inherent properties, and the geometry of the tool, there is a possibility of thermic damage during the process of dry drilling of CFRP [8, 9]. Thus, methods for efficient drilling that guarantee little alteration to the material's mechanical and thermal characteristics have become a focal point of research in the industry.

1.2 Polycrystalline Diamond (PCD) Tool

The material and geometry of the drill are very important factors in ensuring efficient and damage-free machining of CFRP composites. Angles such as tip angle, rake angle, cutting angle, and clearance angle directly contribute to the cutting performance and force generation during drilling operations. Larger tip angles can lead to higher thrust forces and better chip removal but it can also cause greater delamination at the hole exit [10]. Polycrystalline diamond is a synthetic material that disperses small diamond particles in a metal matrix. Due to superior material properties such as hardness, retention of cutting-edge sharpness for prolonged periods, thermal conductivity, superior surface finish, etc., PCD tools are preferred over conventional carbide tools during the machining of abrasive materials such as carbon fibers [11]. A double-tip angle PCD twist drill is used in this study. This tool has two individual cutting edges with point angles, which helps achieve better engagement at the cutting interface and facilitates smooth action. The double margins also provide better stability during the drilling process by reducing the chances of skidding and wandering, which results in more rounded holes, better surface finish, and efficient chip removal [12].

1.3 Cutting Mechanism and Thermomechanical Response during Drilling

The cutting mechanisms in drilling fiber-reinforced polymers differ from traditional materials due to their heterogeneous and anisotropic properties. Cutting forces and temperatures are the key parameters that require optimization to avoid drilling-induced damages such as fiber pull-out, delamination, fiber burning, etc. to obtain quality holes. Drilling forces are attributed as the key factor in drilling-induced defects. The two prominent forces that are most widely analyzed are thrust force and torque. The fibers are tough and brittle whereas the polymer matrix is soft and ductile. These bring about an opposite response on the cutting forces during drilling [13, 14]. According to Bhattacharyya et al. [15] the fibers undertake a large portion of the mechanical load during drilling and the material is cut through stages of fractures of the fibers. The chisel edge of the drill penetrates the workpiece pushing the matrix material away as the main cutting edge of the drill causes fractures in both the fibers and along the interface [16]. The workpiece material can push back on the tool and result in various cutting forces being developed on it [17]. This fiber breakage causes a decrease in both cutting forces at the interface and overall thrust force and torque measurements [18]. Due to it being a constituent of more than one material, response to temperature is a crucial aspect of FRP drilling. The polymer matrix has a considerably lower heat resistance compared to fibers, meaning that the hard glassy state will change into a flexible and highly elastic state and the material qualities will generally decrease when the temperature at the cutting interface goes beyond a particular limit [19]. High temperatures during drilling can cause the material to change its state thus affecting the contact conditions which in turn has an impact on the thrust force and torque measurements recorded. feed and rotational speed are also important contributors to temperature generation. An increase in rotational speed can cause high temperatures at the interface which forms hot localized junctions and softens the workpiece material resulting in a decrease in thrust force [20].

1.4 Thesis Outline

In this study, a predictive drilling model coupled with finite element-based thermal models of the drill and the CFRP laminate is introduced for predicting pressure and tangential stress profiles on the drill tip, the temperature rise on the hole wall surface, and its ensuing effect on the thermomechanical material properties during the dry drilling of CFRP laminate.

Chapter 2 presents a review of the existing literature on the drilling of CFRP and pertinent findings to provide a brief overview of the current state of knowledge on this topic. We aim to provide an assessment of the contributions and limitations of the earlier studies and therefore justify the focus of this study within the range of existing research, highlighting the potential novelty our work brings about.

Chapter 3 illustrates the methods and materials used to conduct this study including the workpiece specimen preparation, the geometry of the tool in use, and the configuration of the drilling experiments for different drilling conditions.

Chapter 4 introduces a predictive thrust force and torque model by considering the drill margin region as a part of the drill tip, split into three sections: the chisel edge, the main cutting edge, and the drill margin region. Pressure and tangential stress, replace the conventional force coefficients, and a temperature-dependent friction coefficient model is proposed to account for the physical interactions at the tool-workpiece interface more precisely, thus providing a better understanding of the distribution of mechanical stresses and thermal effects on material properties at the cutting zone.

In Chapter 5, to compute the heat dissipation ratio based on power generated during drilling, which was taken into consideration in the form of heat fluxes, finite element models were constructed to represent temperatures for both the tool and the workpiece. An inverse approach was employed to determine the heat partition value. The procedure involved comparing the temperature profiles obtained from drilling experiments using thermocouples embedded in the workpiece and the

temperature readings obtained at the drill's exit using an infrared thermal camera, with the predicted temperature profiles obtained from the FE model.

Chapter 6 discusses the effect of feed and rotational speed on the hole wall surface temperature and the pressure and tangential stress profiles developed on the drill tip during drilling by inspecting the different drilling configurations. The behavior of thermomechanical properties of CFRP are analyzed based on experimental observations and the quality of the hole is also investigated after the drilling experiments.

Chapter 2

Literature Review

Analyzing the cutting forces generated during drilling, coupled with the geometry of the drill, both analytically and computationally, to optimize process parameters for better hole quality and cut down manufacturing costs has been a focus in recent years.

Since conducting experiments is not always feasible due to cost, scalability, and lack of optimization opportunities, various mechanistic cutting force models have been introduced to predict forces generated during drilling, and the relevant process parameters have been identified and optimized by performing calibration of these models with relevant experimental data [21, 22, 23, 24, 25]. The tip angle between the axis of the drill and the cutting edges causes the motion of the edges to be at an angle relative to the workpiece material. Thus, the predictive models developed are primarily based on an oblique cutting setting [26, 27, 28]. Diverse types of parameters which are representative of material properties, drilling parameters, and tool geometry have been utilized to accurately predict the cutting forces during the drilling of CFRP laminate composites. The pertinent relationship between the drilling parameters (feed rate and spindle speed) and cutting forces has been established [29, 30]. Force coefficient-based macro-mechanical models are still the preferred option when modeling cutting forces during drilling.

Xiao [22] et al. developed a coupled force prediction model by using process parameters such as friction angle, shear angle, shear strength and rebound height as force coefficients. Karpat et al. [31] proposed a mechanistic model based on force and edge coefficients for predicting thrust force and torque during the drilling of CFRP laminates. Pan et al. [32] distributed the total cutting force into micro-cutting force vectors based on axial, radial, and tangential force coefficients to calculate cutting forces in orbital drilling of CFRP-Ti stacks.

However, only modeling the cutting forces based on the tool geometry and process parameters does not reflect the real scenario of drilling CFRP composites. Cutting temperature is a very crucial factor in drilling as CFRP material's susceptibility to thermal effects can cause significant changes in the contact conditions at the tool-workpiece interface [33]. The temperature at the cutting zone crossing the glass transition temperature (T_g) can cause significant changes in the polymer properties as the highly elastic properties of the material rapidly deteriorate [34, 35]. Literature suggests that crossing the glass transition temperature (T_g) during drilling can lead to a reduction in thrust forces but can increase the chances of delamination due to the physical state of the matrix material changing [36, 37]. As the matrix material gets softer, the fibers are directly exposed to the cutting edges of the tool which can lead to aggregated tool wear [38]. So, analyzing the temperature at the cutting interface becomes paramount for accurately predicting the forces and damage during the drilling of CFRP laminate composites.

Since measuring temperatures at the cutting interface during drilling is an extremely complex task due to the challenging environments present in such high-speed machining operations, numerical modeling has been a popular alternative to address the issue at hand. A myriad of numerical models have been developed to design the physical interactions taking place at the tool-CFRP interface to accurately predict the behavior of the tool and workpiece during drilling experiments [10, 40, 41, 42, 43]. To accurately analyze the conditions at the cutting zone, these models need to be corroborated by experimental data from drilling operations. This brought about studies that coupled the numerical evaluations with experimental data to propose analytical cutting force models that predicted the

forces, damage, and temperature profiles during the drilling of CFRP. Generally, an inverse approach is utilized by using the tool-workpiece thermocouple method and infrared thermography where thermocouples are embedded in the workpiece and the temperature is also measured using thermal cameras to develop FE-based models for the workpiece and the drill and coupling them together helps to predict the conditions at the drill-workpiece interface during drilling [44, 45]. Karpat et al. [45] investigated the borehole quality in CFRP dry drilling by analyzing the contact condition at the interface by proposing a hybrid model, a combination of a time-based analytical and finite-element-based temperature model. The experimental and numerical study of CFRP and Ti stacks using a double-conned drill carried out by Zitoune et al. [46] showed that the use of aluminum at the back end can reduce the delamination at the CFRP hole exit. Bono et al. [47] introduced a FEM-based model for evaluating load generated by heat flux during the drilling of aluminum plates from the thrust force and torque measurements from drilling experiments. A hybrid force and temperature model was developed for accurate predictions of delamination and heat-induced damage in fiber-reinforced polymers by Sadek et al. [48]. To explore the effects of heat on material properties, Santiuste et al. [49] proposed a finite element model for modeling the orthogonal machining of CFRP. Lazoglu et al. [50] introduced a hybrid analytical and FEM-based model for evaluating tool temperature during drilling.

Most of the existing literature on analytical and numerical modeling of the drilling of CFRP laminate composites focuses on the main cutting edge of the drill and its impact on the workpiece material. But, the cutting edge performs shearing action and most of the material is removed in the form of chips. As a result, a very small amount of the heat generated from the cutting is transferred to the material as most of it is carried away by the chips. The hole wall is primarily formed by the drill margin region of the drill since it stays in constant contact with the workpiece surface as shown in Figure 2.1. As stated in Chapter 1, the double-tip angle twist drill has two margins which improves its stability by centering it about the axis during drilling operation and thus providing a better surface finish. The hole diameter is significantly impacted by the design

of the drill margin, and when drilling CFRP, an increase in contact margin may cause laminate damage [51]. The drill margin contributed to almost half of the total torque generated during CFRP drilling according to Bonnet et al. [52]. Fu et al. [53] stated that friction created by contact between the tool margin and the CFRP surface is the cause of high-temperature areas close to the drill exit. According to Shu et al. [54], a smaller contact area between the drill bit and CFRP results in less frictional heat generation at the interface.

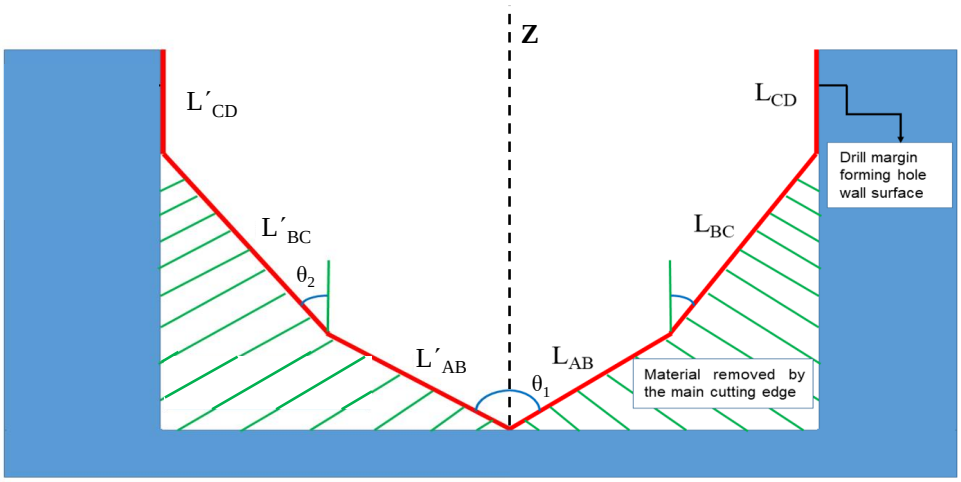

Figure 2.1: Schematics of the tool-workpiece interface during drilling

The drill margin region does not perform any cutting action and only slides against the surface of the workpiece while translating along the axis of the drill. The resistance to motion between two surfaces generates friction. The coefficient of friction is used to quantify this phenomenon. Due to changes in the material properties of polymers around glass transition temperature (T_g), the coefficient of friction is a temperature-dependent property [55]. As per Liang et al. [38], when the temperature gradually increases the matrix in CFRP starts to soften but due to the retention of a good amount of strength, the coefficient of friction is relatively high. Subsequently, as the temperature increases in significant amounts, the state of the polymer starts to change as the material properties deteriorate and at one point the matrix acts like a lubricant which causes a decrease in the coefficient of friction resulting in potential defects. Several studies have been

conducted to investigate the tribological behavior of CFRP composites [38, 56, 57, 58]. Not all material and cutting mechanisms can be accommodated by a single existing coefficient of friction model due to the complexity and diversity of contact conditions in machining [59]. Thus, several friction coefficient models have been proposed over the years for the machining of CFRP [60, 61].

It can be concluded from the above discussions that the drill margin region is an important contributor to torque generation and thermal analysis of drilling, as the continuous interaction at the tool-workpiece interface can be ideal for investigating the behavior of CFRP material during temperature rise. On this account, we will incorporate the drill margin region as a part of the drill tip in our predictive drilling model to estimate the thrust force and torque generated during the drilling of CFRP laminates for various drilling conditions. We will also propose a temperature-dependent coefficient of friction model that accounts for the resistance to motion at the drill margin-CFRP interface. Numerical models for both tool and workpiece will be constructed based on the tool geometry and equivalent contact length at the drill margin-workpiece interface calculated from the experimental thrust force and torque data. The FE models will be calibrated based on the thermocouple and thermal camera temperature measurements. The temperature on the hole wall surface will be investigated and the material's response to thermal effects during drilling will be studied in light of experimental dynamic mechanical analysis results and hole quality observations.

Chapter 3

Experimental Framework

3.1 Work Material Preparation

Toughened epoxy resin unidirectional tapes were used to prepare UD-CFRP (CYCOM 977-2 IM7) laminates for the drilling operation. The fabricated laminate specimen had a diameter and thickness of 75 mm and 13 mm respectively, with a 59% fiber volume. The CFRP laminate comprised of 78 layers of individual laminates with a ply thickness of 0.19 mm, arranged in a repeating sequence of 0° / 45° / 90° / 135° fiber orientation, with the top and bottom layers being 45° and 135° respectively.

3.2 Tool Geometry

The polycrystalline diamond (PCD) ((Walter Titex WCD10) double-tip angle drill with a diameter of 5.6 mm and primary and secondary point angles of 135° and 45°, respectively was used for conducting this study. The schematic of the basic geometry of the polycrystalline diamond (PCD) drill in use is depicted in Figure 3.1(a).

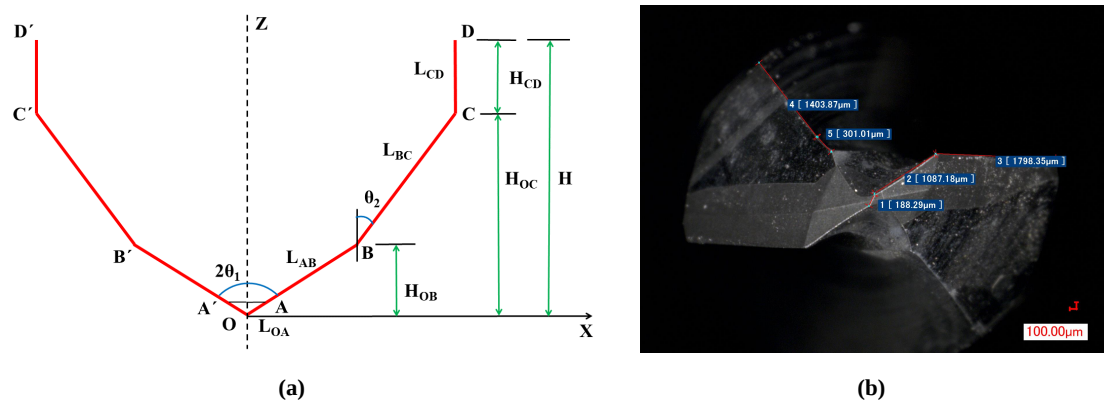

Figure 3.1: Double tip point angle PCD drill geometry: (a) Schematic diagram of geometry of drill; (b) Geometry measurements using Keyence VHX-100 digital microscope.

The chisel edge region is shown in the OA part, and the primary drilling edge region, secondary drilling edge region, and drill margin contact region are shown in the AB, BC, and CD portions, respectively. The lengths of the corresponding regions are L_{OA}, L_{AB}, L_{BC}, and L_{CD}. The primary and secondary tool tip angles are indicated by the numbers θ_1 and θ_2. The drill geometry measurements were performed using the Keyence VHX-1000 digital microscope, as shown in Figure 3.1(b).

3.3 Experimental Set up

All the drilling experiments were performed on a 3-axis CNC machine. The configuration used thermocouples and an associated dynamometer to collect cutting force data and temperature distribution profiles simultaneously as shown in Figure 3.2. Four separate holes with a diameter of 1 mm and a depth of 5 mm were drilled perpendicularly, with respect to the 5.6 mm diameter hole that was to be drilled during experiments, at center-to-center distances of 4 and 6 mm. The thermocouples (K-type, 200–1200°C range) were then inserted into each of the 1 mm holes from the top surface. The temperature data was captured and kept track of during the drilling tests with the help of a data logger.

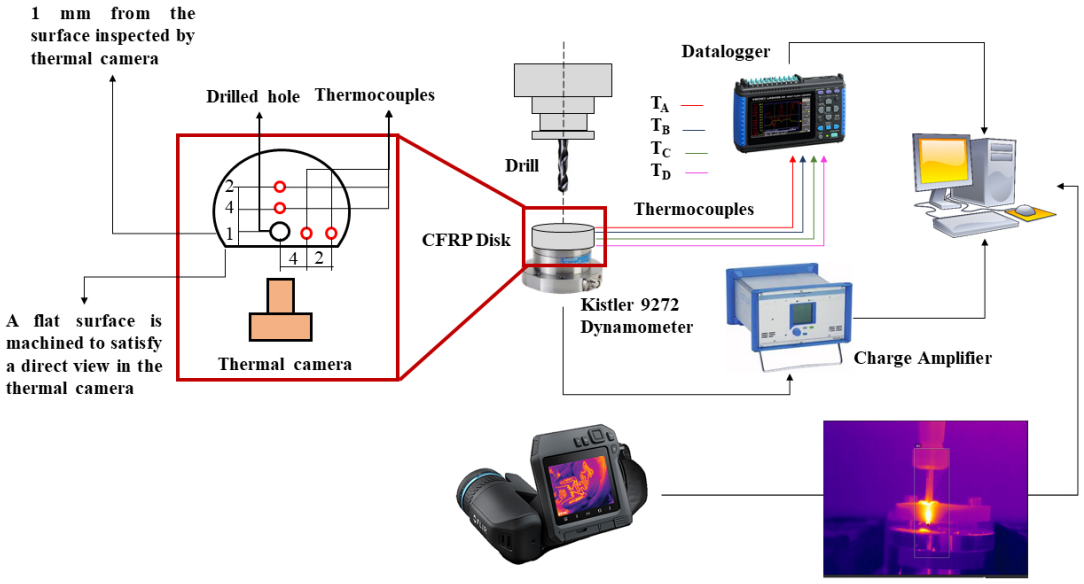

Figure 3.2: Schematics of experimental apparatus for measuring cutting forces and temperature distribution during drilling of thick CFRP laminate.

The setup has two separate parts: the rotational upper fixture for holding the tool and a stable lower fixture for attaching the workpiece using alignment screws. A Kistler 9275 table-type dynamometer, which measures thrust force and torque during the drilling operation, is placed atop the bottom fixture. The experiments have been performed to analyze the effect of feed and rotational speed independently on drill-workpiece interface contact conditions, cutting forces, and subsequent heat partition during drilling. For the rotational speed of 4000 RPM, the feed has been steadily increased from 0.03 mm/rev to 0.05 mm/rev. In contrast, for a fixed feed rate of 120 mm/min, the rotational speed has been raised from 3000 RPM to 5000 RPM. A FLIR infrared (IR) thermal camera is set at a fixed distance from the drilling setup. The center holes drilled by the tool 1 mm from the surface of the workpiece were inspected by the thermal camera and the recorded temperatures were analyzed using FLIR ResearchIR Max 4 software.

Chapter 4

Drilling Process Model

4.1 Drilling Experiment Analysis

The torque and thrust force measurements along with the characteristics time points for various stages of drilling at a feed of 0.03 mm/rev (feed rate of 120 mm/min) at 4000 RPM rotational speed are demonstrated in Figure 4.1. The method of using tool geometry to calculate different time phases of the drilling operation, starting from the point where the tool tip touches the workpiece (Point I) and ending at the point where the drill completely exits the cut (Point VI) was adapted from Karpat et al. [45]

The thrust force and torque both continue to increase as the drill tip enters the CFRP. The thrust force reaches its maximum value at time point II when the chisel, primary, and secondary cutting edge make full contact with the workpiece, however, the torque continues to increase even after the secondary cutting edge finishes its entry into the workpiece. The drill's margin is completely in contact with the workpiece material's surface between periods II and III and continues till the drilling ends at stage VI. The characteristic time point III marks the end of the drill running in phase. The torque reaches its highest value at point III, and from there the thrust force and torque continue to change until Point IV when the tool

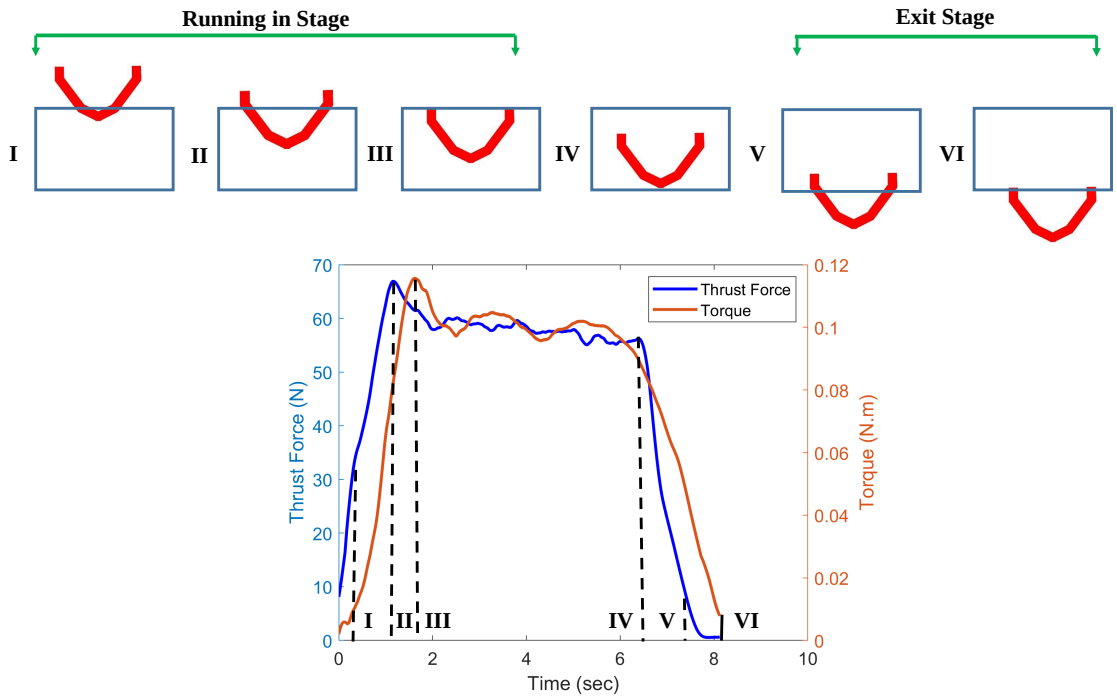

Figure 4.1: Characteristics time point based thrust force and torque measurements for drilling at 0.03 mm/rev feed and 4000 RPM rotational speed.

tip begins to emerge from the hole on the other side. The time interval between time point III and time point IV is termed the stable drilling stage. Changing thrust force and torque indicate significant changes in the contact conditions and material behavior at the tool-workpiece interface during drilling and their impending effect on contact forces. At time point IV, the tip of the tool starts coming out of the hole, which causes the thrust force value to drop to zero at point V sharply. However, since the drill margin is still inside the workpiece at time point V, the torque value does not drop to zero until stage VI similar to the effect between time phase II and III. The interval between time points IV and VI is called the drill exit phase.

The characteristic thrust force and torque values can be measured as a function of feed for all the different drilling conditions and both thrust force and torque increase with increasing feed as shown in Figure 4.2.

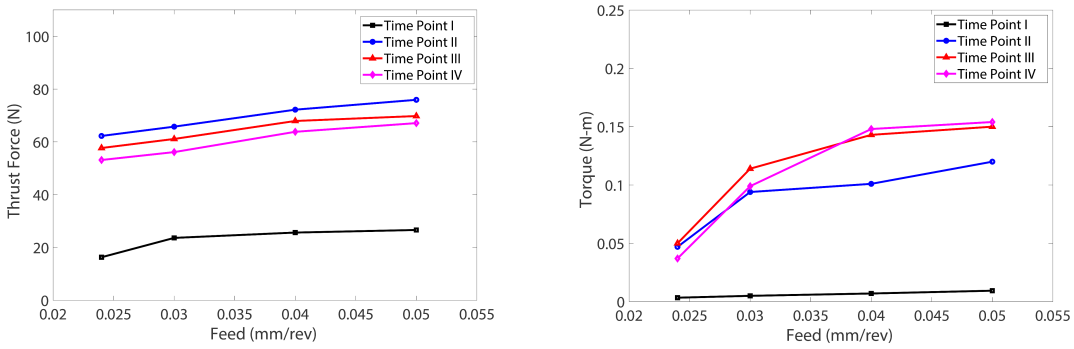

(a) **(b)**

Figure 4.2: Characteristic force measurement: (a) Thrust force; (b) Torque.

4.2 Cutting Force Model

As shown in Figure 3.1(a), the drill tip region can be distributed into three separate sections: the chisel edge region OA, the main cutting edge region AC, and the drill margin region CD. All of these sections and their unique geometrical features contribute to the total thrust force and torque generation during the drilling of CFRP laminates. The chisel edge region does not take part in the cutting mechanism but rather extrudes the workpiece material via penetration. The extrusion force is a significant contributor to the total thrust force generated during the drilling operation. The main cutting edge region AC can be distributed into two sections: the primary cutting edge AB, and the secondary cutting edge BC, which have different point angles θ_1 and θ_2, respectively. The drill margin region does not take part in the cutting mechanism but plays an important role in torque generation because of the sliding action between it and the workpiece surface during hole formation. The cutting force contribution from each section is added to calculate the total thrust and torque values during the drilling operation.

4.2.1 Chisel Edge Region

The geometry of the chisel edge has been studied using a Keyence VK-X100 digital microscope as displayed in Figure 4.3. The geometry represents a cylinder with a blunt radius. This region is responsible for extruding material by acting as a wedge that pushes the workpiece material away. The contact between the chisel edge and the CFRP laminate is assumed to be of Hetrzian nature.

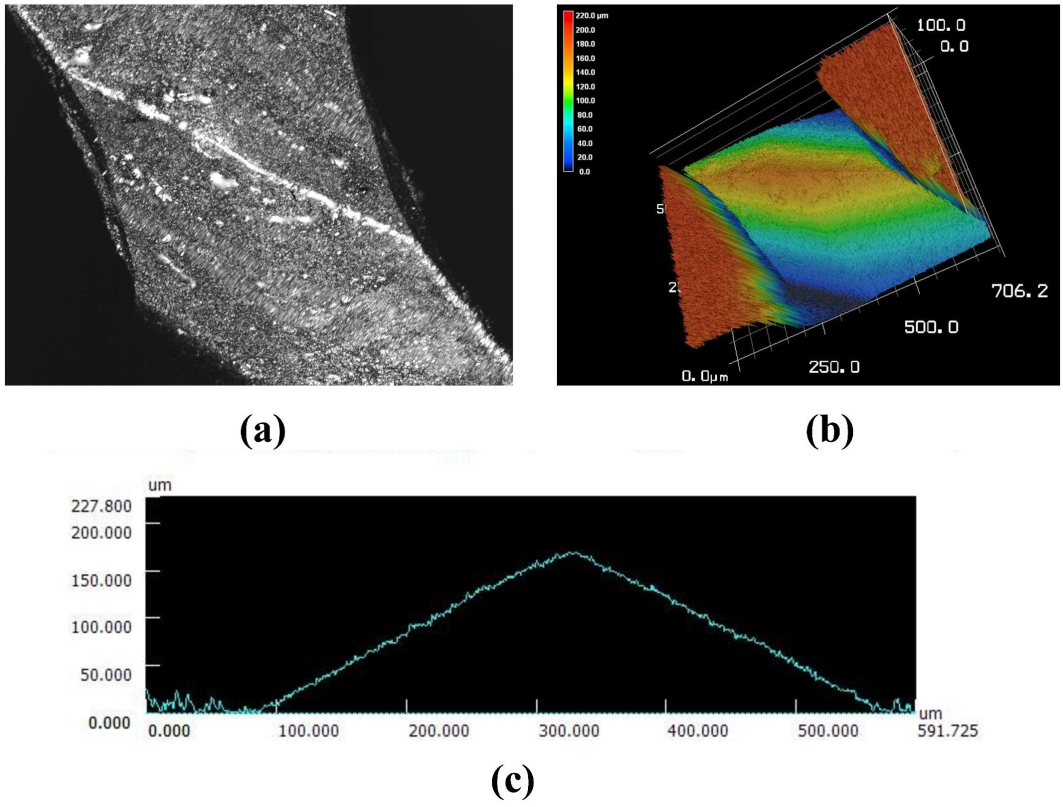

Figure 4.3: Multidimensional surface analysis of chisel edge: (a) 2D grayscale image of the surface. (b) 3D topographical map of the surface. (c) Height variation profile across the surface

According to Hertz Contact Theory, the projected area of contact is rectangular when the chisel edge is parallel to the fiber direction (0°) in the laminate as displayed in Figure 4.4(a). As the chisel edge starts to rotate due to circular motion, the shape of the projected area starts to change as well. The projected area becomes ellipsoidal as exhibited in Figure 4.4(b) and with an increase in

the angle of rotation, the difference between the semi-major axis and semi-minor axis of the ellipse starts to decrease. Finally, when the chisel edge is perpendicular (90°) to the direction of fibers in the laminate, the difference between the semi-major axis and the semi-minor axis is at its lowest and the shape of the projected area resembles a flat-ended circle as shown in Figure 4.4(c) [62]. So, it can be conferred that the maximum contact area condition at the chisel edge and laminate interface arises when the chisel edge is parallel to the fiber direction and the minimum contact area condition arises when the chisel edge is perpendicular to the fiber direction.

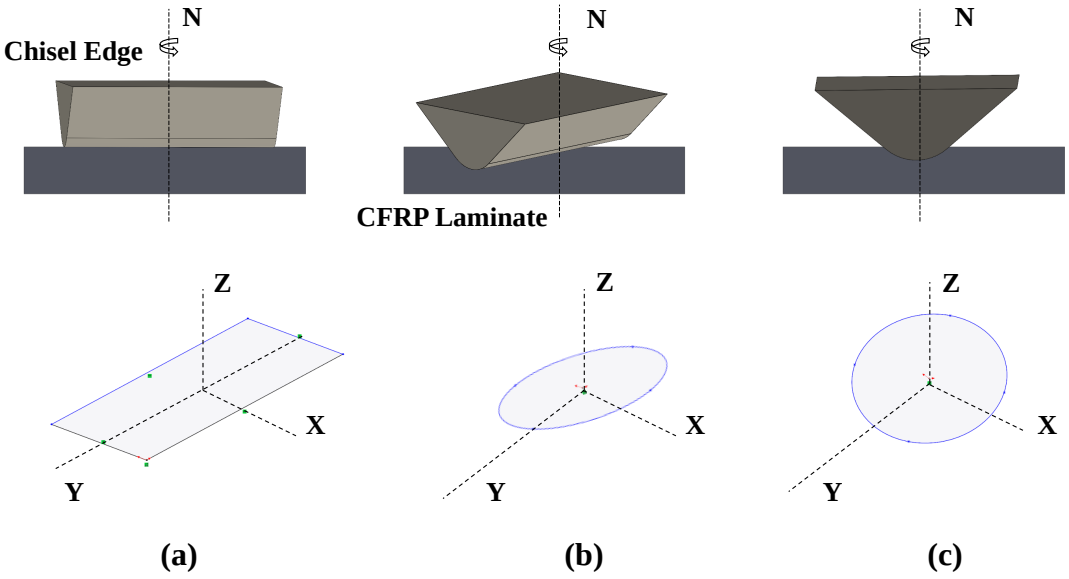

Figure 4.4: Change of contact state and the projected area between chisel edge and CFRP laminate: (a) Parallel to the fiber direction (0°). (b) At an angle with the fiber direction. (c) Perpendicular to the fiber direction (90°).

Due to the rotation of the drill at a very high speed, accurate measurement of the contact area at any given instance is difficult. For ease of calculation of the extrusion force generated by the chisel edge, we will be assuming a constant contact area at the chisel edge-workpiece interface, despite it varying for every individual rotation. We will not be taking into account the insignificant torque contribution from the chisel edge since the extrusion force almost entirely contributes to the total thrust force generated by the chisel edge because of axial

penetration into the workpiece. The thrust force generated by the chisel edge can be calculated using Equation 4.1.

$$F_{ch} = P_{max} \times A_{ch} \tag{4.1}$$

Here, F_{ch} is the thrust force generated at the chisel edge, A_{ch} is the contact area at the chisel edge and workpiece interface, and P_{max} is the maximum pressure intensity acting on the contact area.

4.2.2 Main Cutting Edge

Since the two sections of the main cutting edge: primary and secondary cutting edge have different point angles which are not right angles, an oblique cutting framework adapted from the literature [63, 64, 65, 66] has been considered in this study. The main cutting edge and drill margin are discretized into small elements (dl) which removes an elemental chip with an area (dA), and the unit thrust force and torque on each element can be calculated by the proposed model. Oblique cutting is characterized by a unit normal force that acts normal to the rake face of the relevant edge and a unit frictional force that acts in the tangential direction. They are expressed as a function of pressure (P) and tangential stress (τ) respectively, along the main cutting edge of the drill as described in Equations 4.2 and 4.3.

$$dF_n(l) = P_{AC}(l) \times dl \times \frac{f}{2} \sin\theta \tag{4.2}$$

$$dF_f(l) = \tau_{AC}(l) \times dl \times \frac{f}{2} \sin\theta \tag{4.3}$$

Here, P_{AC}, τ_{AC} are the pressure and tangential stress acting on the entire main cutting edge region, l is the incremental elemental length on the main cutting edge, f is the feed, and θ is the point angle.

P(l) and $\tau(l)$ are the unknowns in the aforementioned equations. They vary along the drill tip. Let us assume that the variation of peak pressure and tangential stress on each section of the drill tip can be defined using Equations 4.2 and 4.3, where parameter b controls the variation of them along the tip of the drill.

$$P(l) = P_{\max} \times \left(1 - \frac{l}{L}\right)^{b} \tag{4.4}$$

$$\tau(l) = \tau_{\max} \times \left(\frac{l}{L}\right)^{b} \tag{4.5}$$

Here, P_{max} is the maximum pressure on each section of the drill tip, τ_{max} is the maximum tangential stress on each section of the drill tip, l is the incremental elemental length of drill tip, L is the total length of the drill tip and b is an arbitrary parameter that represents variation along each section of the drill tip for both pressure and tangential stress.

The elemental drilling forces acting on a particular edge in the drill coordinate system pertinent to the drilling operation are the cutting force dF_{cut} acting in the opposite direction of the cutting velocity of the relevant edge, the thrust force dF_{thru} normal to the plane that accommodates the cutting force, and lastly, the lateral force dF_{lat} acting perpendicular to both cutting and thrust forces as illustrated in Figure 4.5. The unit normal and frictional force defined in the oblique cutting setup are then decomposed along the drill coordinate system with the help of a transformation matrix, which is a function of point angle, web angle, cutting angle, inclination angle, normal rake angle, and chip flow angle as demonstrated in Equation 4.6. Apart from the point angle, all the other angles are considered dynamic parameters. The details of calculating the angles for the drill tip can be found in the Appendix A section.

$$\begin{bmatrix} dF_{lat} \\ dF_{cut} \\ dF_{thru} \end{bmatrix} = \begin{bmatrix} \cos\eta \sin i \sin(\alpha_n - \sin\eta \cos i) & \cos\alpha_n \sin i \\ \cos\eta \cos i \sin(\alpha_n - \sin\eta \sin i) & \cos\alpha_n \cos i \\ \cos\eta \cos\alpha_n & -\sin\alpha_n \end{bmatrix} \begin{bmatrix} dF_n \\ dF_f \end{bmatrix} \tag{4.6}$$

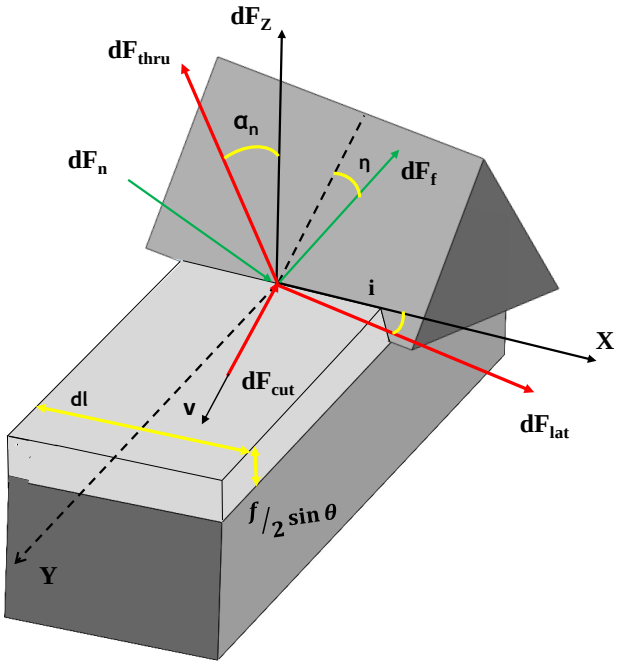

Figure 4.5: Elemental drilling forces experienced by the unit workpiece in an oblique cutting framework

Here, i is the inclination angle, α_n is the normal rake angle and η is the chip flow angle.

The unit thrust force and torque generated by each element on the main cutting edge during the drilling process can be estimated by Equations 4.7 and 4.8.

$$dF_Z = dF_{thru}\frac{\cos(\beta)\sin\theta}{\cos i} - dF_{lat}\frac{\cos\theta}{\cos i} \tag{4.7}$$

$$dTr_Z = r_i \times dF_{cut} \tag{4.8}$$

Here, dF_Z is the elemental thrust force, dTr_Z is the elemental torque, β is the web angle, and r_i is the drill radius for each incremental element.

Summing all the elements on the apt edges will add up to the total thrust force and torque generated by the main cutting edge, as shown in Equations 4.9 and 4.10.

$$F_Z = 2\sum_{n=1}^{N} dF_Z \tag{4.9}$$

$$Tr_Z = 2\sum_{n=1}^{N} dTr_Z \tag{4.10}$$

Where F_Z is the total thrust force, Tr_Z is the total torque, and N is the total number of unit elements on the cutting edge individually.

4.2.3 Drill Margin Region

Many frictional and tool characteristics contribute to the complex contact conditions at the tool-workpiece interface [67]. As shown in Figure 4.6, the drill margin is the area of the drill that comes into contact with the surface of the material between time points II and III and can be computed using the pertinent feed rate and the time difference between these two characteristic time points for any drilling conditions. A line contact between the drill margin and the hole's surface is considered to simplify the modeling of the moving heat source for the FE modeling of the drilling process. The contribution of the drill margin in the contact region can be approximated based on the contact length. This is termed the drill margin contact length and can be determined using Equation 4.11.

$$L_{CD} = \Delta t \times F_r \tag{4.11}$$

Here, L_{CD} is the drill margin contact length, F_r is the feed rate (mm/min) and Δt is the time difference between the two time points II and III.

The drill margin contact lengths for different drilling cases are listed in Table 4.1. The evaluated contact lengths are much higher than the feeds, making drill margin contact conditions an important factor in CFRP drilling.

Table 4.1: Drill margin contact length calculation.

Feed (mm/rev)	**RPM**	**Feed rate (mm/min)**	**Contact length (mm)**
0.024	5000	120	1.1
0.04	3000	120	1.7
0.03	4000	120	0.9
0.04	4000	160	1.2
0.05	4000	200	1.4

The drill margin region CD does not perform any cutting action but still takes part in generating torque. Since there is only sliding contact at the drill margin-workpiece interface, no tangential stress is generated in this region. The unit normal force can be calculated similarly to the cutting edge region by considering it as a function of pressure (P) along the length of the drill margin. However, due to no cutting mechanism and the margin sliding against the workpiece surface, the unit frictional force is evaluated by considering the coefficient of friction at the tool-workpiece interface, which is a function of temperature and the unit normal force. The unit normal and frictional force can be evaluated with the help of Equations 4.12 and 4.13.

$$dF_{n_{CD}}(l) = P_{CD}(l) \times w \times L_{CD} \tag{4.12}$$

$$dF_{f_{CD}}(l) = \mu(T) \times dF_{n_{CD}} \tag{4.13}$$

The sensitivity of CFRP to heat makes temperature a key parameter in the drilling process. A complex tribosystem is created due to the repeated rubbing of the drill margin with the hole's surface being formed [68]. Drilling operation can be generally divided into three stages: the running-in stage, the stable stage, and the exit stage. Initial contact during the running in stage causes the coefficient of friction to be higher due to the real contact area being considerably smaller than the apparent contact area [38]. When the temperature crosses the glass

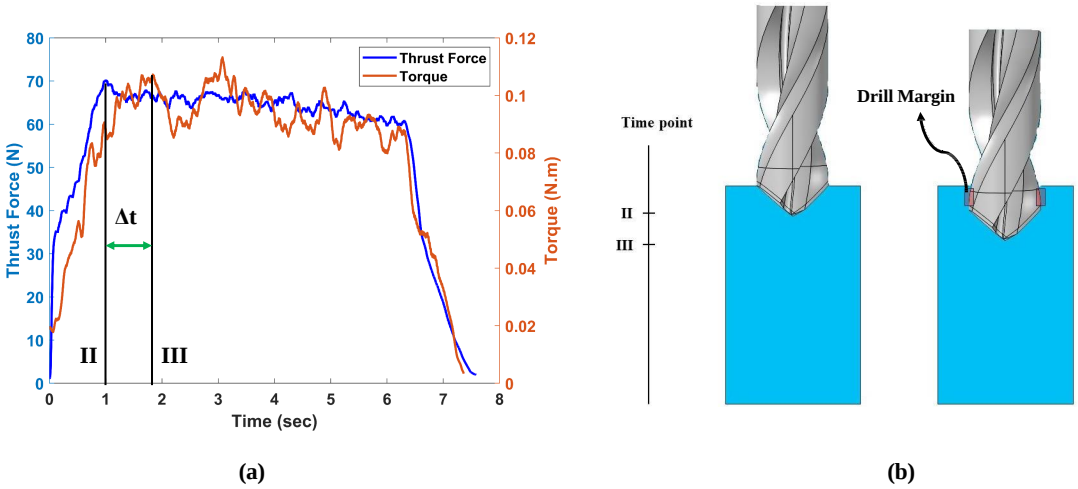

Figure 4.6: Drill margin length measurement: (a) Identifying characteristic time points from thrust force and torque measurements for drilling at 0.04 mm/rev feed and 3000 RPM rotational speed. (b) Characteristic time points for drill margin detection.

transition temperature (T_g), the semi-crystalline structure of CFRP changes by allowing large-scale movement of polymer chains which change the behavior of the material by making it softer [19]. Softer material causes the resistance to sliding at the interface to be less, resulting in the coefficient of friction dropping at temperatures higher than the glass transition temperature (T_g). The glass transition temperature of epoxy resin CYCOM 977-2 is 212°C at 10°C/min according to the manufacturer's catalog. Based on the thermal effects on the constitutive material behavior and existing literature on the evaluation of the coefficient of friction of CFRP, this study considers a temperature-dependent coefficient of friction model as shown in Equation 4.14.

$$\mu(T) = A \times e^{-\left(\frac{\frac{(T-T_r)}{(T_g-T_r)}}{B}\right)^2} + C \quad \text{if } T_{\min} \leq T \leq T_{\max} \tag{4.14}$$

Here, T_r is the room temperature, T_g is the glass transition temperature, T is the temperature at the tool-workpiece interface and A, B, and C are the arbitrary parameters that represent the variation in behavior of coefficient of friction.

The elemental drilling forces on the drill margin can be calculated using Equation 4.6. Although the main contribution to the thrust force comes from the chisel edge and main cutting edge region, the friction between the margin and the hole wall of the workpiece from continuous rubbing due to the rotation of the drill generates a frictional force, a component of which acts in the axial direction contributing towards thrust force generation. However, compared to the high-speed rotation (3000-5000 RPM), the axial translation of the drill termed feed is insignificant making the thrust force contribution from the drill margin region negligible. The unit torque from the drill margin region can be determined by Equations 4.15.

$$dTr_{CD} = r_i \times dF_{f_{CD}} \tag{4.15}$$

The total torque Tr_{CD} on the drill margin can be evaluated similarly to the main cutting edge.

Chapter 5

Model-Based Evaluation of Temperature Distribution in Drilling Processes

5.1 Workpiece and Tool design

A cylinder-shaped section of the CFRP laminate measuring 16 mm in diameter and 13 mm in height was modeled for FE analysis. Repeating layers of UD-CFRP laminates with 0°, 45°, 90°, and 135° fiber orientations constitute the layered structure. A 5.6 mm hole with a depth equivalent to the height of the laminate was created at the center of it The temperature distribution profile will be measured by placing 4 different points inside the workpiece model perpendicular to each other at a distance of 4 mm and 2 mm respectively as illustrated in Figure 5.1.

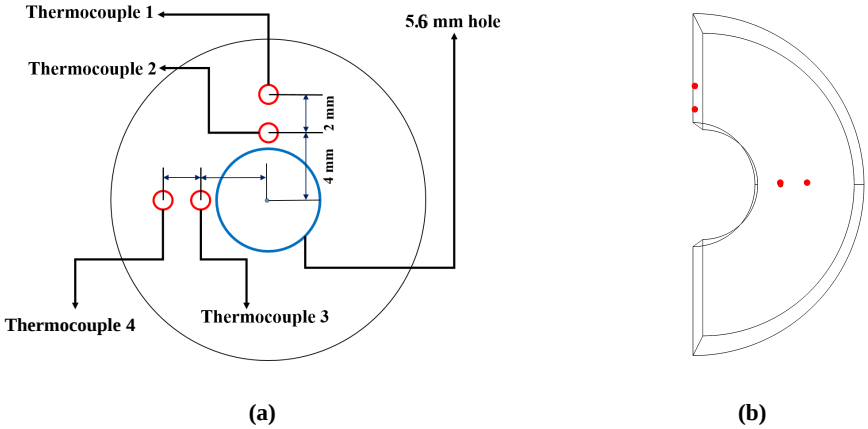

Figure 5.1: Placing measuring points on the hole's surface for temperature measurements: (a) Schematics of the measuring points. (b) Temperature profile obtained from each measuring point.

Table 5.1: Material Properties of CFRP

Parameter	**Expression**
Density (ρ)	1588
Longitudinal thermal conductivity (k_1)	$0.013 \times T + 2.95$
Transverse thermal conductivity (k_2)	$0.007 \times T + 1.5$
Through thickness thermal conductivity (k_3)	$0.0007 \times T + 0.5744$
Specific heat capacity (C_p)	$0.0029 \times T - 0.0817$

Table 5.2: Material Properties of Polycrystalline Diamond (PCD)

Parameter	**Expression**
Density (ρ)	3830 kg m^{-3}
Thermal conductivity (k)	560 W m^{-1} K^{-1}
Specific heat capacity (C_p)	500 J kg^{-1} K^{-1}

The heat capacity of the laminate is not significantly affected by the orientation of the fibers [69]. The in-plane thermal conductivities of the fibers vary with changes in plane directions, but it is independent of the angle at which the fiber is placed in the laminate [70].

Using the rule of mixture, which is based on the weighted average of the densities of the constituent materials, the total density is calculated. The temperature-based material properties adapted from the literature [69] can be found in Table 5.1. Using the tool geometry measurements from the digital microscope, a 5.6 mm diameter polycrystalline diamond (PCD) drill was designed. The properties of PCD material shown in Table 5.2 were adopted from the literature [71, 72].

5.2 Heat Source Modeling and Power Calculation

To simulate the drilling process, the moving heat source designed is a time-varying heat flux that rotates along the hole wall at a constant speed and translates through the hole. The total equivalent contact length is identified, taking into account any influence of the main cutting edge alongside the drill margin during the drilling operation. The heat flux input into the FE model is a function of the heat source, drill time, and geometry of the workpiece. It displays the heat produced by the equivalent contact length at the drill tip that is in continuous contact with the hole wall surface on both sides of the drill. The schematic presented in Figure 5.2(a) illustrates the geometrical cross-section of the cylindrical hole drilled in the laminate. The green directional arrow indicates the direction in which the heat flux generated is rotating along the hole surface while translating through it.

The complex contact conditions at the tool-workpiece interface during high-speed drilling, make accurate modeling of cutting conditions very challenging, more so in the case of PCD tool-based drilling of CFRP composites owing to

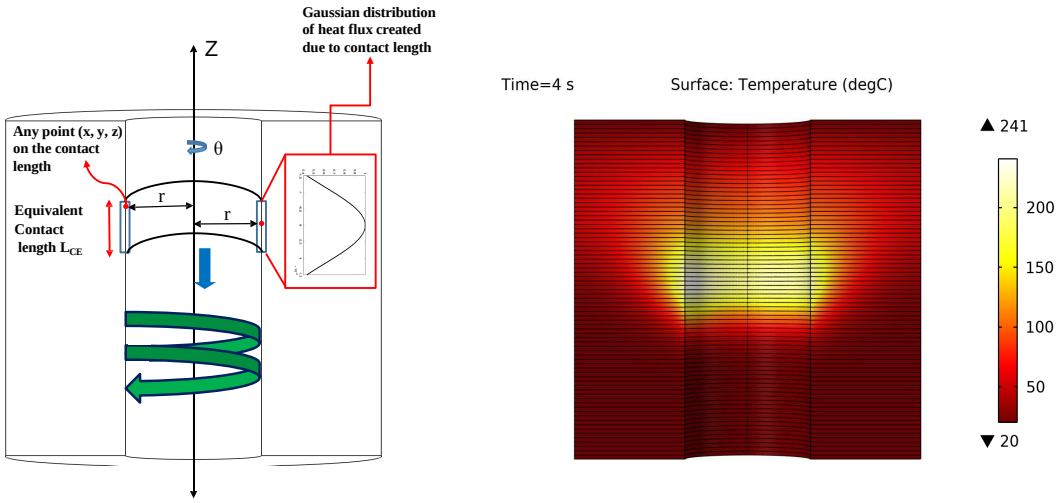

Figure 5.2: FE model of drilling operation using a rotational translatory heat source: (a) Schematics of the moving heat source prompted heat flux. (b) Drilling at 0.03 mm/rev feed and 4000 RPM rotational speed.

the intricate physical structure and material properties, [73]. To obtain a more accurate prediction for temperature profiles in the workpiece during the drilling operation, the heat flux needs to be represented in terms of both spatial (physical space) and temporal (time) distribution [74]. To address spatiality, a Gaussian profile was chosen because of the ease of implementing it in our FE model and the flexibility in calibrating the proposed model by iteratively matching the predictive FEA temperature distribution profile with experimental temperature distribution profiles obtained from the embedded thermocouples during drilling. Equation 5.1 presents the equivalent contact length-based heat source modeled as a ring-type Gaussian distribution [75].

$$H_S = e^{-(a/L_{CE})} \tag{5.1}$$

Here, H_S is the Gaussian distribution, L_{CE} is the total equivalent contact length, and the distance between the center and the ring's outer edge is termed

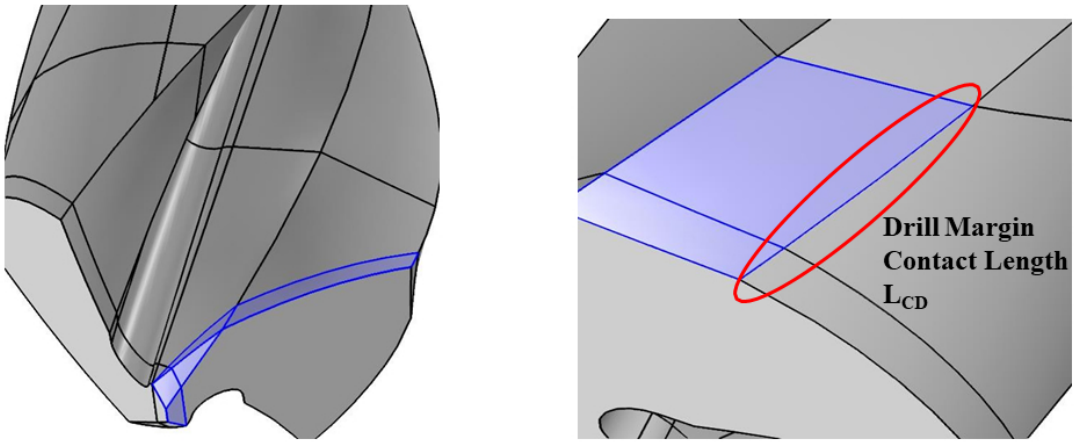

Figure 5.3: Contact area on tool during drilling: (a) Main cutting edge. (b) Drill margin

a.

As shown in Figure 5.2(b), the tool and chip load on the workpiece during the drilling operation is considered equivalent to the transitory heat source. Equation 5.2 is used to compute the time-based power distribution to the workpiece during the drilling process based on the combination of the ring-type heat flux and the model geometry.

$$P_w(t) = 2 \int_0^a \int_0^{2\pi} Q_w \, a \, d\theta \, da \tag{5.2}$$

Here, the power distributed to the workpiece is expressed as P_w, and Q_w represents the heat flux input into the FE model.

During the drilling experiments, time-based thrust force and torque measurements were collected. Equation 5.3, which was adapted from the literature by [45], allows us to evaluate the total drilling power needed during drilling as a function of time using these measurements.

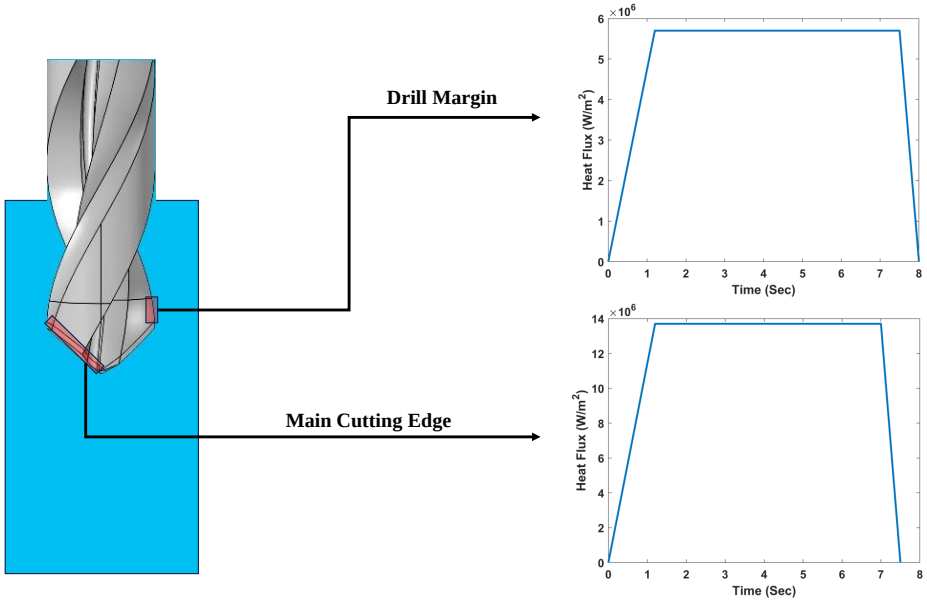

Figure 5.4: Heat fluxes presented as time-based step functions.

$$P(t) = F_z(t) \times f \times N + Tr(t) \times N \times \frac{2\pi}{60} \tag{5.3}$$

F_z and Tr present the thrust force and torque values and f and N are the feed and rotational speed respectively.

Equation 5.4 illustrates making use of the tool power (P_t) distributed over the contact area (A_c) of the drill tip to calculate the heat flux generated on the aforementioned region.

$$Q_t(t) = \frac{P_t(t)}{A_c} \tag{5.4}$$

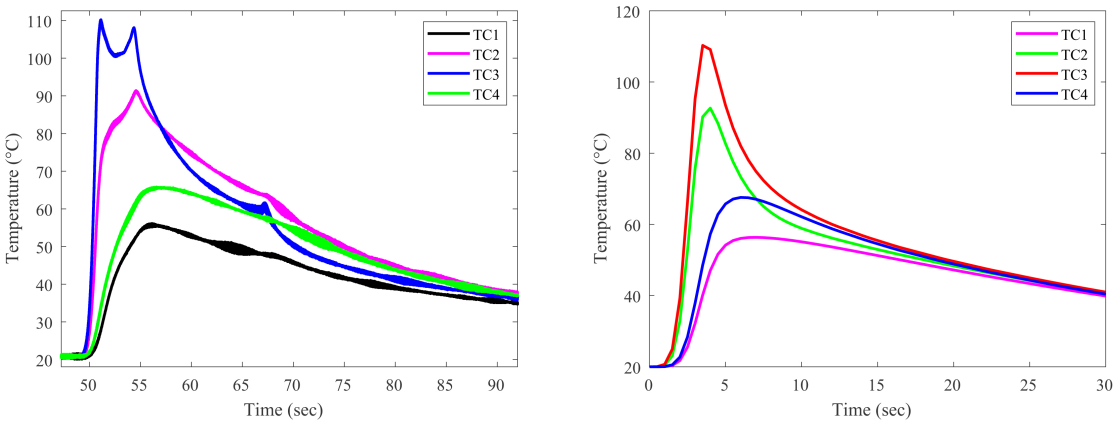

Figure 5.5: Temperature profiles from embedded thermocouples during drilling at 0.03 mm/rev feed and 4000 RPM rotational speed: (a) Experimental profile. (b) FE model profile.

The drill margin contact area is determined using the contact length (L_{CD}) and the drill's periphery, as indicated in Figure 5.3(b), while the contact area of the primary cutting edge is computed based on tool geometry data depicted in Figure 5.3(a). The drill margin and the primary cutting edge each have their own computed heat fluxes. The time phase at which the tool exits the hole propagates to zero contact force at the edges, as seen in Figure 4.1. So, time-based step functions derived from the time points identified in Figure 4.1 were linked with the heat fluxes to emulate the thermal load created on the drill during experiments, as illustrated in Figure 5.4.

5.3 Heat Partition Evaluation

The total drilling power is associated with the integral heat generation during drilling, overcoming friction at both the cutting edge and the drill margin, and removing material in the form of chips. During the drilling process, some of the power is lost as chips. Heat is transferred from the remaining power into the material and tool. Heat partition to the workpiece (η_w) and heat partition to the tool (η_t) are the terms used to describe the percentage of total heat that is dissipated into the workpiece and tool, respectively. The material, tool, and chip heat partition values add up to 1. It is evaluated by comparing the drilling operations' experimental and simulated temperature distribution data [45, 76].

The FE model uses an initial Gaussian heat flux that is designed by an approximated total equivalent contact length (L_{CE}) to calculate the temperature distribution profile. Figure 5.5 shows the temperature profiles derived from the FE model for different drilling scenarios and experimental drilling operations using the thermocouples placed inside the sample during drilling.

The calibration of the heat flux is performed by iteratively minimizing the discrepancy between the experimental temperature measurements and predictions by the FE model for the thermocouples at every time point. The comparison between the experimental and FE-based temperature profiles for drilling at 0.03 mm/rev feed and 4000 RPM rotational speed, acquired from thermocouples, is shown in Figure 5.6. The findings are in good agreement, and the variation in the profiles could be attributed to damage, issues with the sensors, or the thermocouples being displaced from their intended locations [77]. Equation 5.2 is then modified to take into account the assessed heat flux to calculate the power applied to the workpiece. The heat partition to the workpiece (η_w) is the percentage of total drilling power that is distributed to the workpiece.

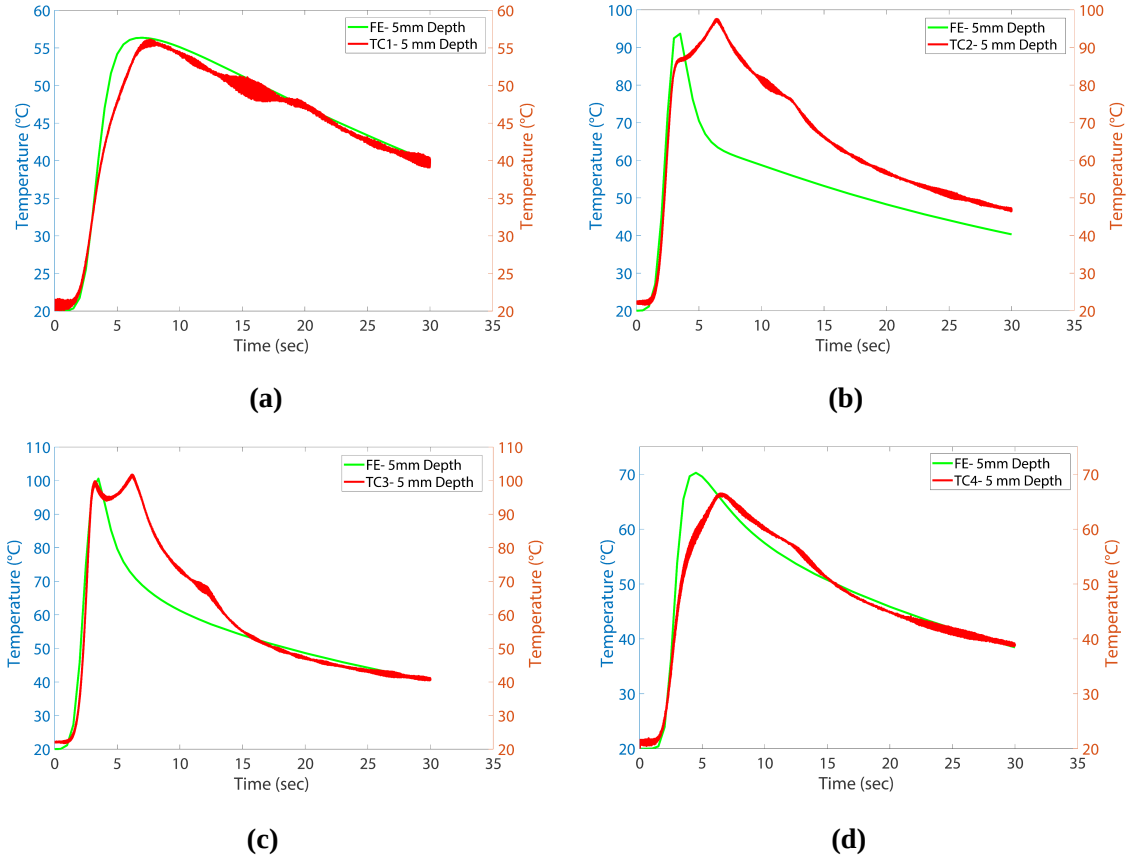

Figure 5.6: Temperature measurements from embedded thermocouples during drilling at 0.03 mm/rev feed and 4000 RPM rotational speed: (a) Thermocouple 1. (b) Thermocouple 2. (c) Thermocouple 3. (d)Thermocouple 4.

The remaining drilling power is subjected to the tool (P_t) and the chips. Equation 5.4 is used to compute the heat flux acting on the drill tip. The tool's FE model is then updated with the estimated heat fluxes as time-based step functions. The finite element framework, as illustrated in Figure 5.7, can be used to predict the temperature distribution on the tip of the tool during the drilling process. The tool tip temperature at the hole exit during the experimental drilling operation is measured using infrared thermography. The temperature during drilling is measured by observing the visual images of heat levels captured by a thermal camera that is positioned at a fixed distance as depicted in Figure 5.8.

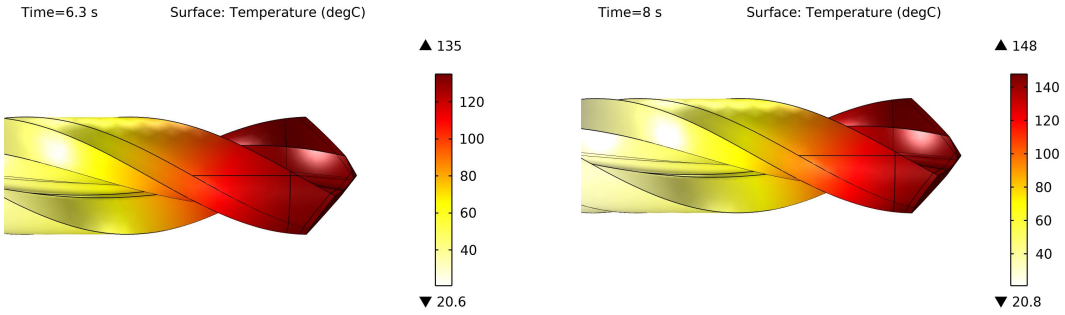

(a) **(b)**

Figure 5.7: Tool tip temperatures at the hole exit: a) Drilling at 0.05 mm/rev feed and 4000 RPM rotational speed; (b) Drilling at 0.024 mm/rev feed and 5000 RPM rotational speed.

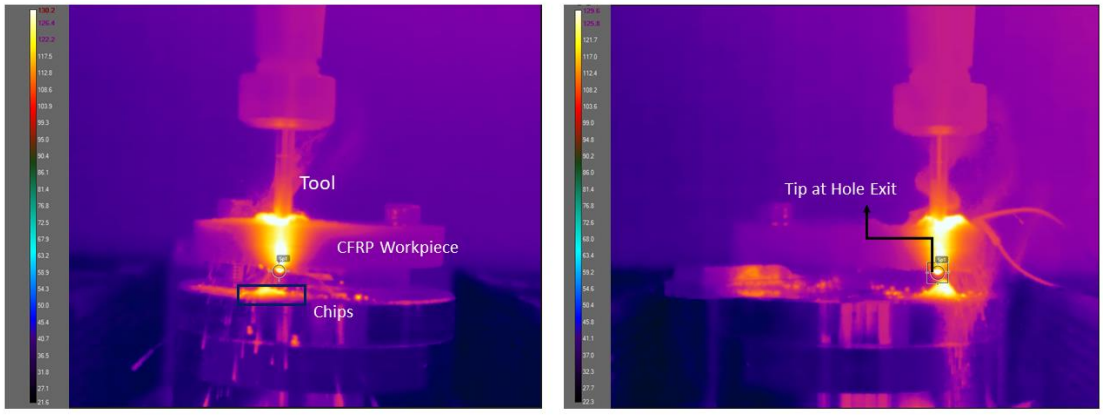

(a) (b)

Figure 5.8: Infrared thermal camera temperature measurements at hole exit:(a) Drilling at 0.05 mm/min feed and 4000 RPM rotational speed; (b) Drilling at 0.04 mm/rev feed and 3000 RPM rotational speed.

Table 5.3: Tool tip temperature results

Feed (mm/rev)	**RPM**	**Feed Rate (mm/min)**	**Experimental temperature (°C)**	**FE model temperature (°C)**
0.024	5000	120	144.3	148
0.04	3000	120	129.6	130
0.03	4000	120	130	133
0.04	4000	160	130.2	128
0.05	4000	200	135	131

Table 5.3 lists the temperature predictions from the FE model and the experimental tip temperature observations. With an error margin of about 5%, the simulated and experimental tool tip temperatures at the hole exit are in good agreement with each other. Heat distribution to the tool (η_t) is the fraction of total drilling power dispersed to the tool.

Table 5.4: Heat partition results

Feed (mm/rev)	**RPM**	**Feed Rate (mm/min)**	**Heat partition to workpiece (η_w)**	**Heat partition to tool (η_t)**
0.024	5000	120	0.29	0.47
0.04	3000	120	0.37	0.30
0.03	4000	120	0.31	0.38
0.04	4000	160	0.26	0.42
0.05	4000	200	0.23	0.50

The time-averaged heat partition values for the workpiece and the drill for different drilling conditions were identified as listed in Table 5.4.

Chapter 6

Results and Discussions

The pressure and tangential stress profiles on the drill tip during drilling can be estimated by calibrating the predictive thrust force and torque values calculated from the coupled cutting force and finite element model with experimental data. A better comprehension of the mechanical stresses generated on the drill's cutting edge is necessary to determine process parameters during drilling to obtain better-quality holes. The temperature-dependent material properties also affect the contact conditions between the drill and the workpiece. The temperature profiles developed on the hole wall surface in the FE model are employed to analyze the behavior of temperature-dependent material properties and their corresponding contribution to the thrust force and torque generation during different drilling conditions.

6.1 Hole Wall Temperature

From the heat partition results in Chapter 5, it is observed that a portion of the total heat generated at the interface is distributed to the workpiece. CFRP composites are generally considered to be a poor conductor of heat due to their low thermal conductivity [78]. This causes the culmination of heat on the hole wall, which can lead to thermal damage on the surface. Thus, assessment of the temperature on the hole wall becomes crucial in investigating the response of the material to rising temperatures and subsequent cutting force predictions.

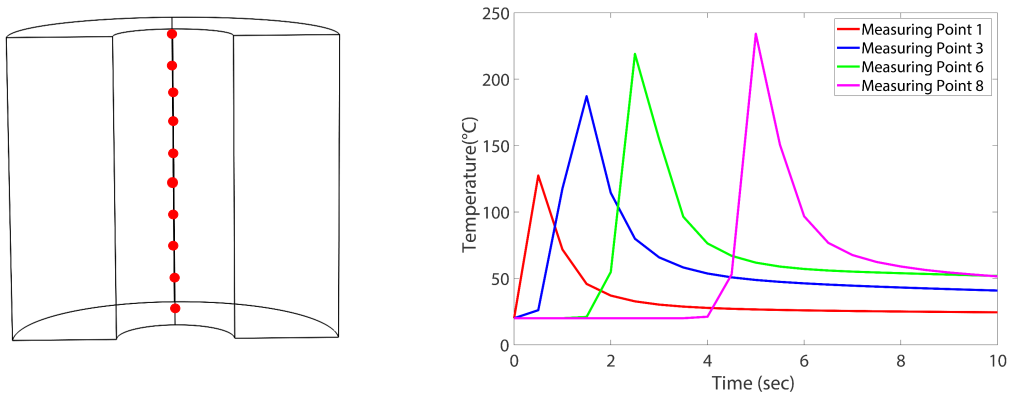

Figure 6.1: Placing measuring points on the hole's surface for temperature measurements: (a) Schematics of the measuring points. (b) Temperature profile obtained from each measuring point.

The hole wall temperature was measured by placing 10 separate evenly distributed points on the surface of the hole in the direction of the axial movement of the drill as exhibited in Figure 6.1. Each point records its temperature profile as the ring-type heat source translates along the hole while rotating. The maximum temperature estimated at each of these points can be attributed to the temperature generated by the equivalent contact length at the workpiece drill-margin interface during that particular stage of the drilling operation. The hole wall temperature profiles for different drilling cases are illustrated in Figure 6.2.

During the running in stage, initial engagement between the tool and the workpiece causes rapid temperature rise. Once full contact is achieved, the drilling process becomes stable and it can be corroborated by the comparatively gentler increasing trend observed in the temperature profile. As the tool starts to penetrate the workpiece on the other side, marking the beginning of the drill exit stage, there is a rapid decrease in temperature, which is conversely similar to the running in stage. The partition of heat to the workpiece decreases with increasing feed as shown in Table 5.4 with more heat being transferred to the tool. This results in the hole wall temperature decreasing as well with increasing feed as depicted in Figure 6.2(b), (c), and (d) respectively. Change in the rotational speed also affects the temperatures on the hole wall, as an increase in speed leads to temperature rise while the opposite corresponds to a decrease in temperature as exhibited in Figure 6.2(a) and (e) respectively.

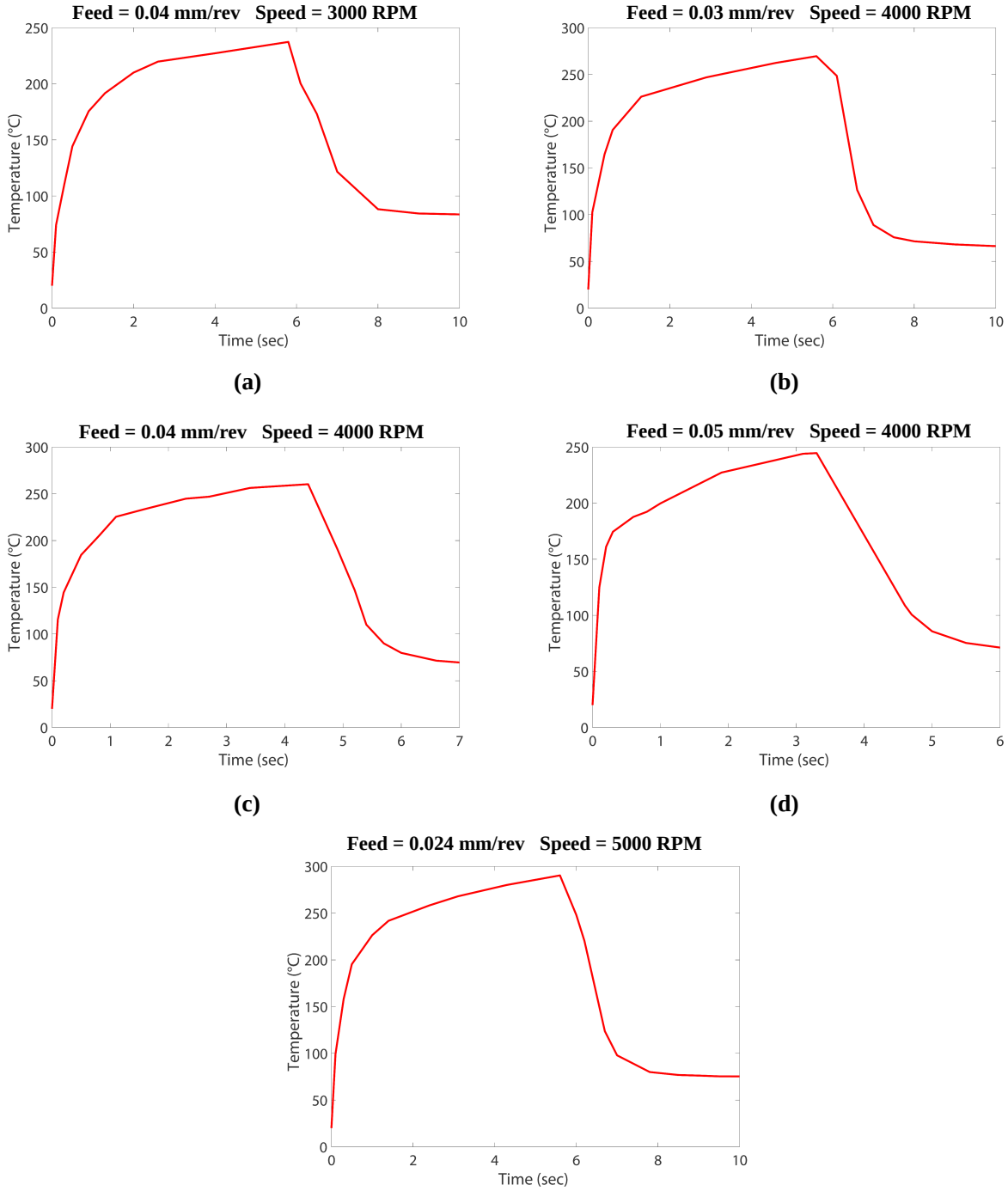

Figure 6.2: Temperature profile on hole wall of CFRP laminate: a) Drilling at 0.04 mm/rev feed and 3000 RPM rotational Speed. (b) Drilling at 0.03 mm/rev feed and 4000 RPM rotational speed. (c) Drilling at 0.04 mm/rev feed and 4000 RPM rotational speed. (d) Drilling at 0.05 mm/rev feed and 5000 RPM rotational speed. (e) Drilling at 0.024 mm/rev feed and 5000 RPM rotational speed.

6.2 Drilling Process Parameter Identification

The thrust force and torque contribution from each region of the drill tip can be identified by introducing characteristic time points representing the different stages of the drilling operation, adapted from Karpat et al. [45]. The pressure and tangential stress values along each incremental length of the drill tip at every moment during drilling can be estimated by calibrating the predictive thrust force and torque values to match the experimental data. The calibration is performed by iteratively minimizing the percent error between predictive and measured force values at every characteristic time point to calculate the unknown parameters.

For drilling at 0.03 mm/rev feed and 4000 RPM rotational speed, the contact area at the chisel edge and workpiece interface varies between 0.0046 mm2 and 0.0456 mm2 for every individual rotation. A constant contact area of 0.008 mm2 has been assumed for the ease of calculating the extrusion force generated by the chisel edge during drilling. As stated previously, the drill margin does not perform any cutting action but slides against the workpiece surface. The resistance to sliding action is termed as the coefficient of friction and it can be calculated by employing the hole wall surface temperature and Equation 4.14 from Chapter 4.

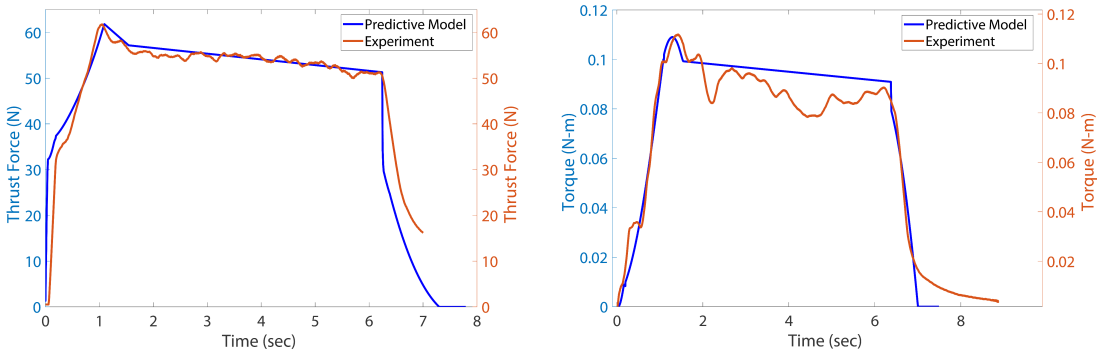

Figure 6.3: Thrust force and torque comparisons for drilling at 0.03 mm/rev feed and 4000 RPM rotational speed: (a) Thrust Force. (b) Torque.

Figure 6.3 shows the comparison between the model and experimental thrust force and torque models for drilling at 0.03 mm/rev feed and 4000 RPM rotational speed. The pressure and tangential stress profiles on the tip of the drill can now be evaluated.

Because of the different geometrical features of the double-point angle drill tip as exhibited in Figure 3.1(a), each region has its own distinctive pressure and tangential stress profile. During the running in period, as the chisel edge region OA begins to penetrate the workpiece material, the concentrated extrusion force over a small contact area causes the pressure on it to be the maximum (1800 MPa). The hole wall temperature predictions show a prompt rise in temperature during the initial engagement. This alters the elastic modulus of the workpiece material, causing a change in the contact conditions between the drill and the workpiece, leading to an increase in contact area. This increasing area causes the pressure to decrease along the cutting edge. Since it is a double-point angle drill, the cutting edge comprises two distinctive cutting edges with separate geometry, namely the primary cutting edge region AB and the secondary cutting edge region BC. Figure 6.4(a) shows the decreasing pressure profile along both cutting edges. Since the drill margin-workpiece interface only accounts for sliding contact, the pressure in the region CD is the lowest among all the regions, as presented in Figure 6.4(b).

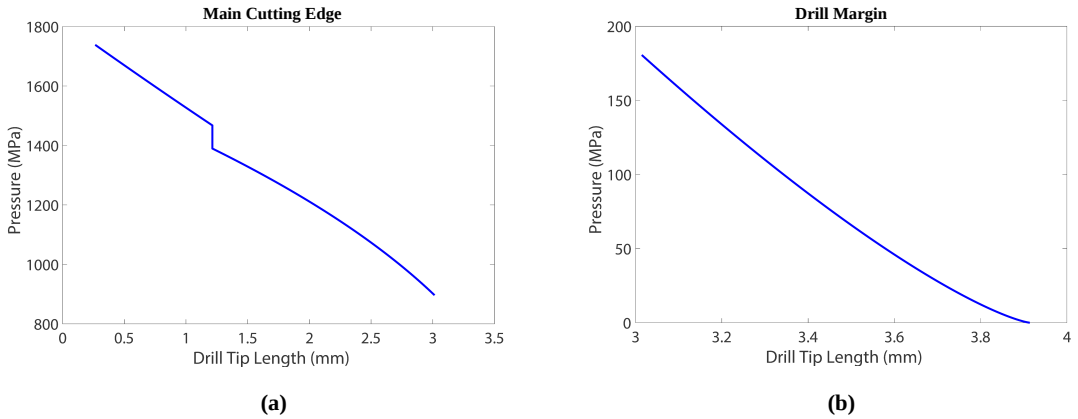

Figure 6.4: Pressure profile on drill tip for drilling at 0.03 mm/rev feed and 4000 RPM rotational speed: (a) Main cutting edge region. (b) Drill margin region.

As for the tangential stress on the drill tip, since the extrusion force generated by the chisel edge region OA primarily acts in the axial direction, there is a very negligible amount of force acting in the tangential direction, amounting to a trivial amount of tangential stress on the chisel edge, as shown in Figure 6.5(a). The main cutting edge responsible for material removal through shearing produces a significant amount of tangential stress, which reaches its maximum value at the end of the secondary cutting edge BC. Similar to the pressure profile on the cutting edges, the tangential stress profiles are also distinctive for both regions, as exhibited in Figure 6.5(b). There is no tangential stress present on the drill margin because no cutting mechanism is in effect.

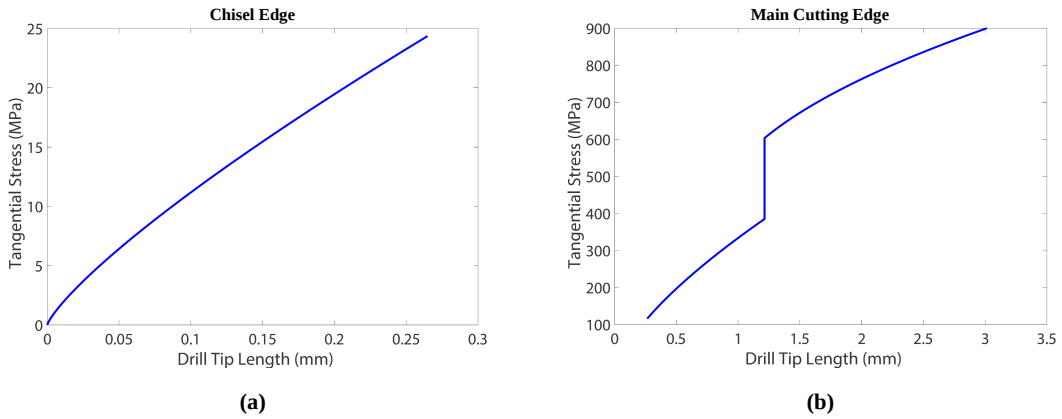

Figure 6.5: Tangential stress profile on drill tip for drilling at 0.03 mm/rev feed and 4000 RPM rotational speed: (a) Chisel edge region. (b) Main cutting edge region.

The comparison between the predictive and experimental cutting force values and corresponding stress profiles on the drill tip for drilling at a rotational speed of 4000 RPM and a feed of 0.04 mm/rev are illustrated in Figures 6.6, 6.7 and 6.8. Similarly, Figures 6.9, 6.10 and 6.11 depict the aforementioned profiles for a drilling configuration of 0.05 mm/rev feed and 4000 RPM rotational speed.

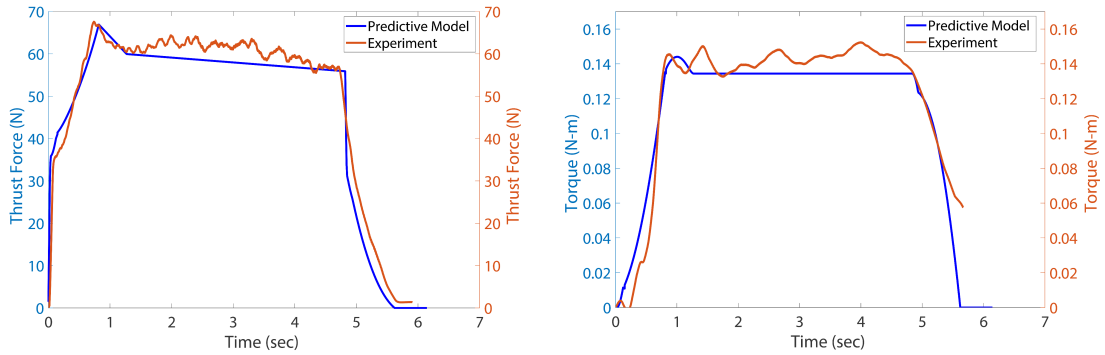

Figure 6.6: Thrust force and torque comparisons for drilling at 0.04 mm/rev feed and 4000 RPM rotational speed: (a) Thrust Force. (b) Torque.

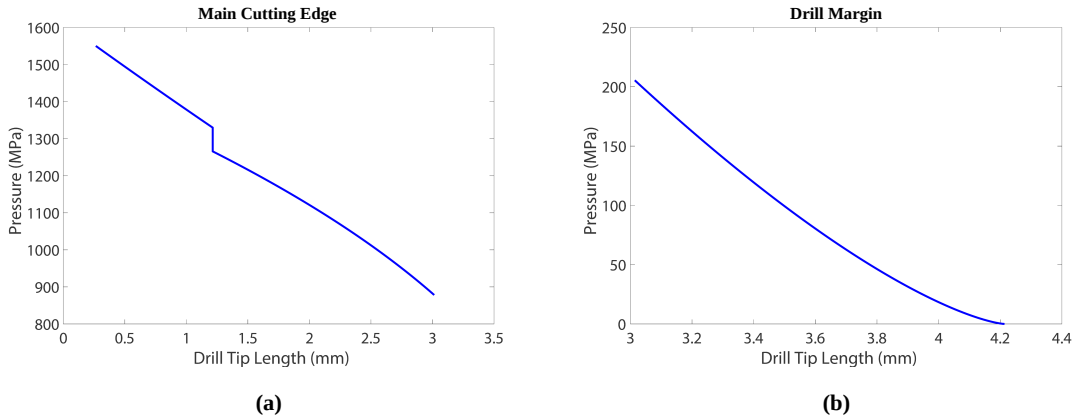

Figure 6.7: Pressure profile on drill tip for drilling at 0.04 mm/rev feed and 4000 RPM rotational speed: (a) Main cutting edge region. (b) Drill margin region.

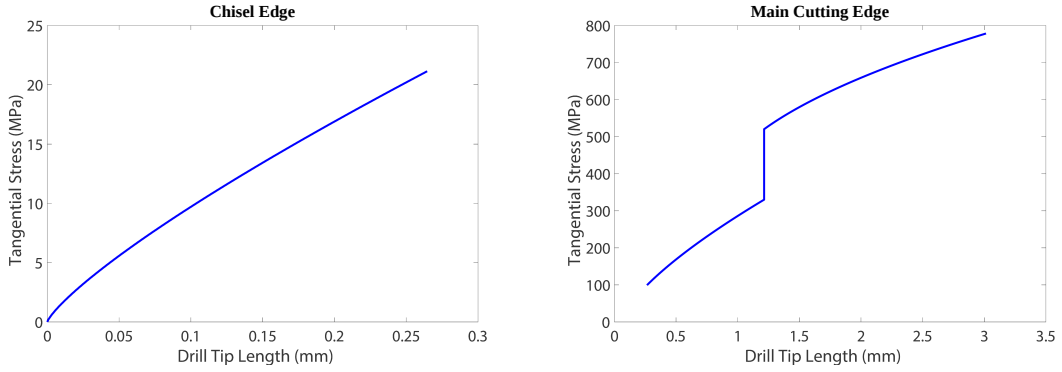

Figure 6.8: Tangential stress profile on drill tip for drilling at 0.04 mm/rev feed and 4000 RPM rotational speed: (a) Chisel edge region. (b) Main cutting edge region.

Higher feeds cause the uncut chip area to increase, enabling the cutting-edge radius to have less effect during cutting, which results in more tool engagement and efficient machining. The increase in chip thickness also leads to a decrease in specific cutting energy due to the energy required for cutting spreading over a larger volume resulting in less cutting energy requirement per unit volume, which leads to higher cutting forces [79]. The energy required to remove a unit volume of material decreases, this induces less pressure and tangential stress to develop on the cutting edge compared to drilling at a lower feed of 0.03 mm/rev.

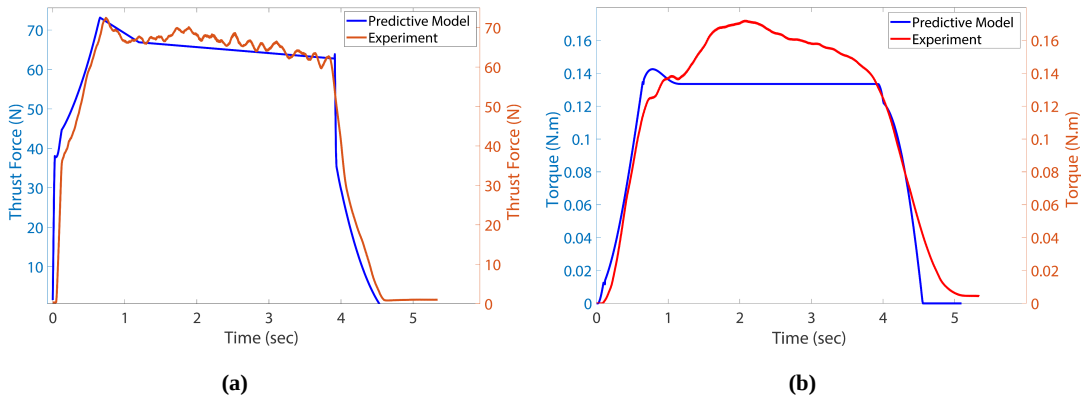

Figure 6.9: Thrust force and torque comparisons for drilling at 0.05 mm/rev feed and 4000 RPM rotational speed: (a) Thrust Force. (b) Torque.

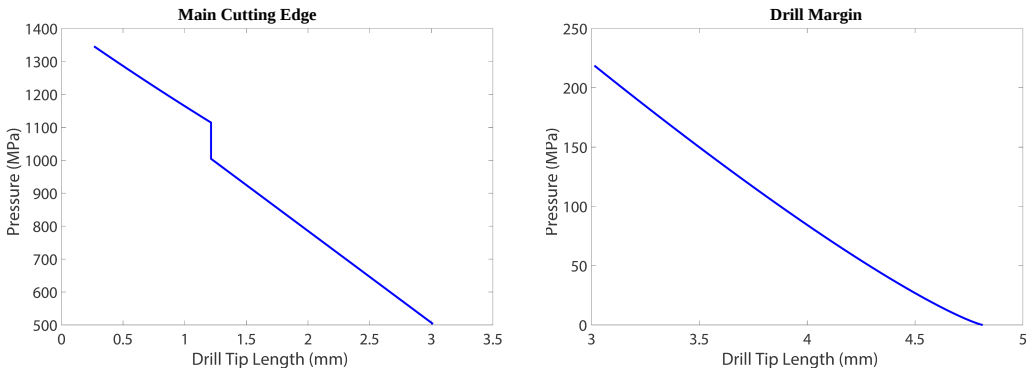

Figure 6.10: Pressure profile on drill tip for drilling at 0.05 mm/rev feed and 4000 RPM rotational speed: (a) Main cutting edge region. (b) Drill margin region.

However, the pressure on the drill margin follows a reverse trend as the increase in feed causes it to rise. Larger feed causes more tool engagement which leads to an increase in the pressure at the drill margin region. In the case of drilling at high feeds, the effect of high-pressure development on the drill margin is visible during the stable stage of drilling as there is evidence of chip accumulation. Higher pressure at the drill margin traps chips during evacuation causing an increase in the contact length at the interface. Trapped chips can increase friction and resistance resulting in higher cutting forces. The substantial impact of chips being present at the interface is observed for the highest feed of 0.05 mm/rev as it creates a notable difference between the predicted and experimental torque values during the stable stage drilling.

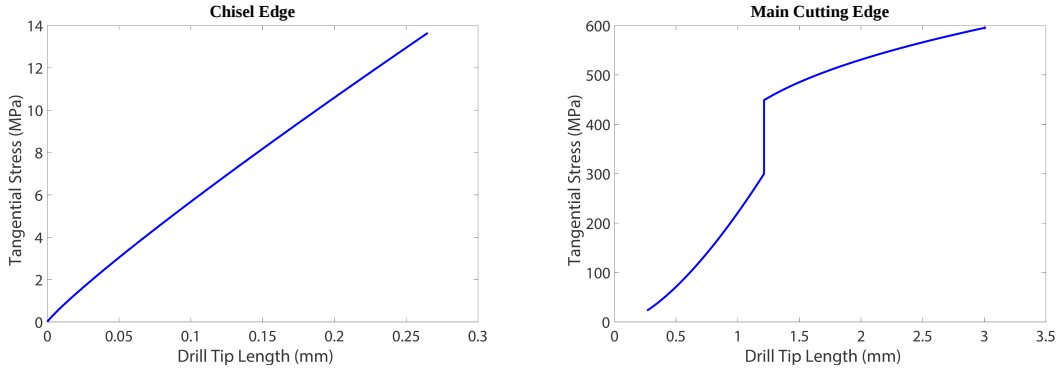

(a) **(b)**

Figure 6.11: Tangential stress profile on drill tip for drilling at 0.05 mm/rev feed and 4000 RPM rotational speed: (a) Chisel edge region. (b) Main cutting edge region.

Chip clogging can also lead to an incline in centripetal force and contribute to additional torque formation due to the chip's adherence to the surface of the drill from strain hardening [80]. Thus, an abrupt increase in the experimental thrust force and torque measurements is observed during the stable stage of drilling. The difference between the predictive and experimental models in this region can be attributed to this phenomenon.

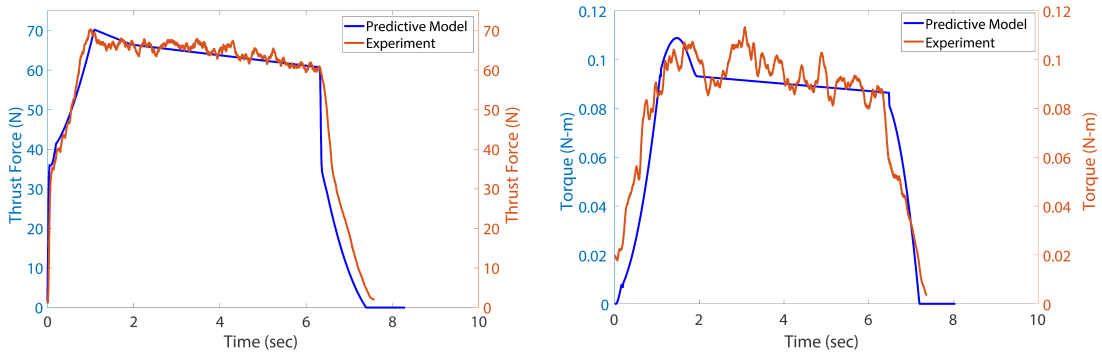

(a) **(b)**

Figure 6.12: Thrust force and torque comparisons for drilling at 0.04 mm/rev feed and 3000 RPM rotational speed: (a) Thrust Force. (b) Torque.

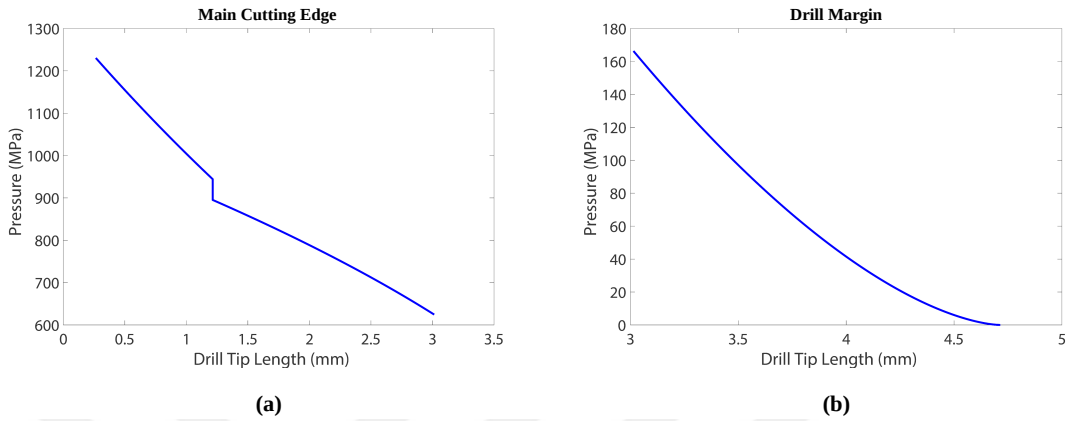

Figure 6.13: Pressure profile on drill tip for drilling at 0.04 mm/rev feed and 3000 RPM rotational speed: (a) Main cutting edge region. (b) Drill margin region.

Rotational speed also has an effect on the cutting forces during drilling. Higher rotational speeds significantly reduce the cutting forces generated during drilling due to the formation of smaller chips [81]. The comparison between the predictive and experimental thrust force and torque measurements and the corresponding stress distributions for drilling at 0.04 mm/rev feed and 3000 RPM rotational speed are shown in Figures 6.12, 6.13 and 6.14 and for 0.024 mm/rev feed and 5000 RPM rotational speed are exhibited in Figures 6.15, 6.16 and 6.17 respectively.

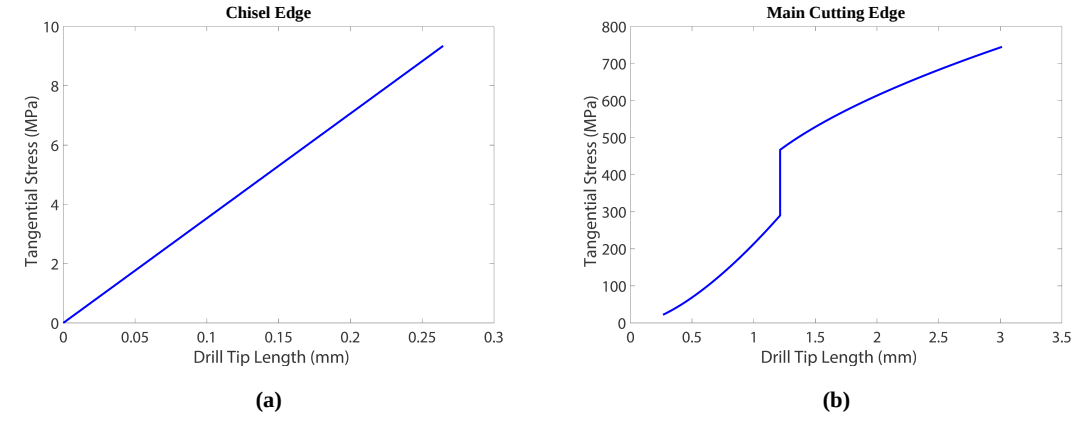

Figure 6.14: Tangential stress profile on drill tip for drilling at 0.04 mm/rev feed and 3000 RPM rotational speed: (a) Chisel edge region. (b) Main cutting edge region.

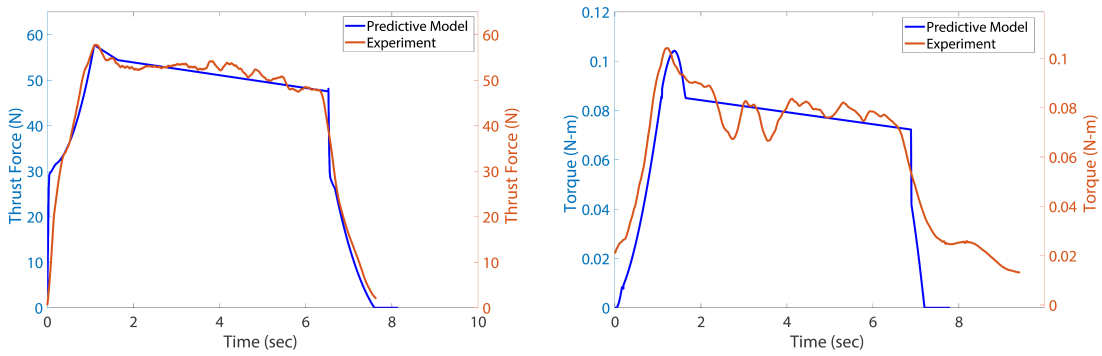

Figure 6.15: Thrust force and torque comparisons for drilling at 0.024 mm/rev feed and 5000 RPM rotational speed: (a) Thrust Force. (b) Torque.

Chip clogging effects are also observed in the case of drilling at 3000 RPM during the stable stage, which causes a discrepancy between the thrust force and torque predictions and experimental data during the stable stage drilling.

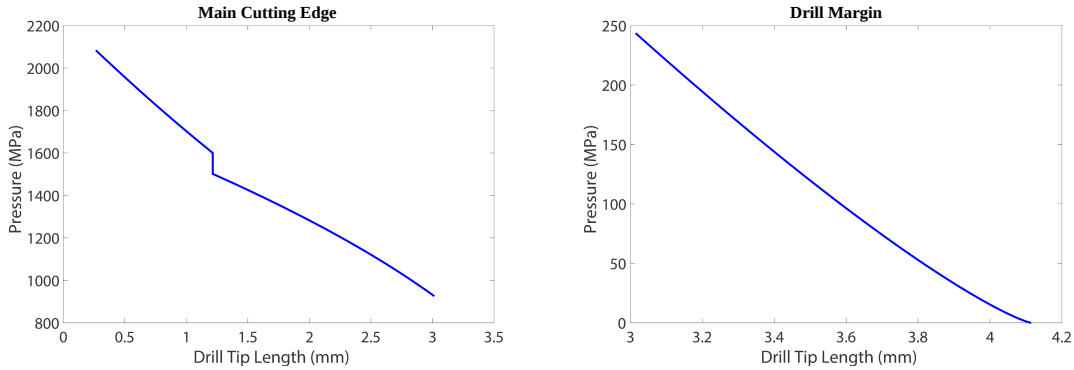

Figure 6.16: Pressure profile on drill tip for drilling at 0.024 mm/rev feed and 5000 RPM rotational speed: (a) Main cutting edge region. (b) Drill margin region.

The thrust force and torque measurements show a decreasing trend with increasing speed which is in line with the trend observed in the literature [82]. Due to a low feed of 0.024 mm/rev being used at 5000 RPM, the specific cutting energy increases which increases the pressure and tangential stress values as illustrated in Figures 6.16 and 6.17. At a rotational speed of 3000 RPM, as the feed is increased to 0.04 mm/rev the pressure and tangential stress decrease significantly as reported previously. Higher pressure at the drill margin region is also observed at higher rotational speeds.

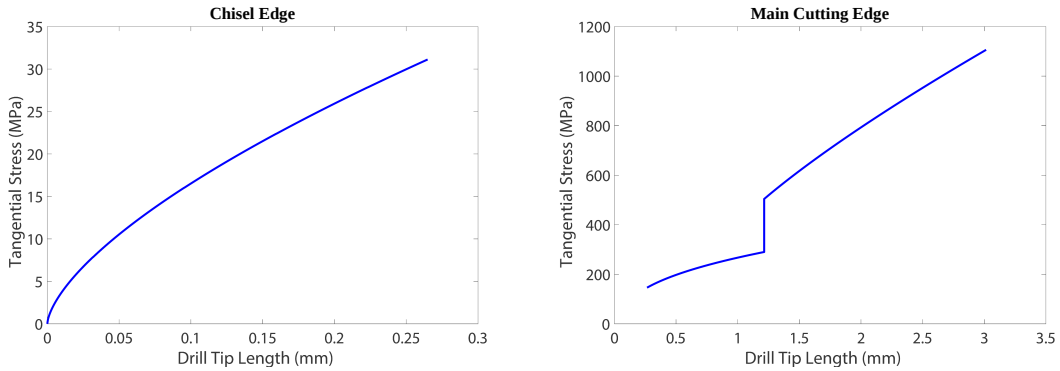

Figure 6.17: Tangential stress profile on drill tip for drilling at 0.024 mm/rev feed and 5000 RPM rotational speed: (a) Chisel edge region. (b) Main cutting edge region.

So, the importance of process parameter (feed and speed) variance and its influence on the development of stress at the tool-workpiece interface is explored in this section. Also, the change in pressure and tangential stress is more significant on the secondary cutting edge compared to the primary cutting edge which indicates a greater engagement at the cutting zone due to greater length. More engagement increases the area of contact generating higher cutting forces in this region. While the stress analysis was performed based on only discrete time points, it lays the groundwork for a potential study of stress evolution at the interface for every instance of the total drilling process.

6.3 Effect of Temperature on Material Properties during Drilling

The influence of temperature on material properties can be studied by coupling the predictive drilling model with the hole wall temperature rise from the workpiece FE model. The coefficient of friction on the drill margin region during drilling has been calculated based on the temperature profile obtained from the hole wall surface. The analysis of experimental thrust force and torque measurements in Section 4.1 revealed that the drill margin is fully inside the workpiece at characteristic time point III, which can be termed as complete engagement of the drill tip and the end of the running in period. The interval between characteristic time points II and III can be assigned as the time required for the drill margin region to acquire full contact with the workpiece surface. Hole wall surface temperature evaluation at that specific time interval estimates the temperature to be in the range of the initial glass transition temperature (T_{g_0}) of CFRP as reported by Karpat et al. [45]. The change in polymeric material around the glass transition temperature (T_g) has been discussed previously in several chapters. As the material becomes flexible due to changes in its molecular properties, the storage modulus of the material decreases and it becomes easier to machine due to less resistance being offered to deformation. This causes a decrease in the peak cutting forces with increasing drilling time as observed in all the thrust force and torque measurements from different drilling cases. The maximum pressure on the drill margin is obtained at characteristic time point III when the torque reaches its highest value. The pressure profile on the drill margin continues to decrease as the temperature increases with incremental drilling time up until the start of the drill exit stage. To simplify the visualization of changes in pressure profiles on the drill margin, only the peak value at each drill time point has been considered. The maximum pressure and coefficient of friction on the drill margin-workpiece contact region are illustrated as a function of temperature for all the drilling configurations in Figure 6.18.

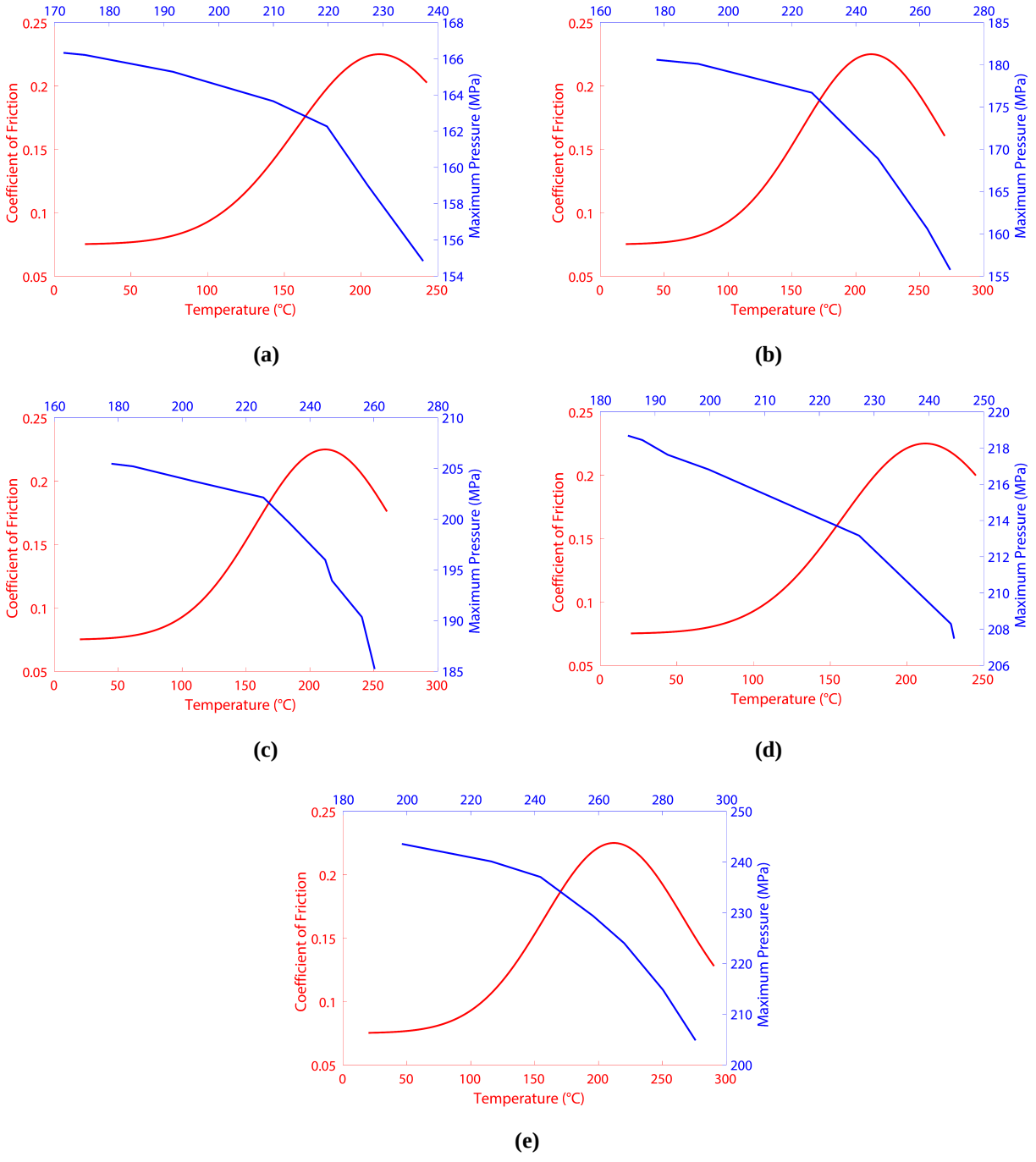

Figure 6.18: Maximum pressure and coefficient of friction on the drill margin-workpiece interface with rising temperature in stable stage drilling: a) Drilling at 0.04 mm/rev feed and 3000 RPM rotational speed. (b) Drilling at 0.03 mm/rev feed and 4000 RPM rotational speed. (c) Drilling at 0.04 mm/rev feed and 4000 RPM rotational speed. (d) Drilling at 0.05 mm/rev feed and 5000 RPM rotational speed. (e) Drilling at 0.024 mm/rev feed and 5000 RPM rotational speed.

The maximum pressure as a function of temperature resemble the variation of storage modulus in dynamic mechanical analysis conducted on CFRP laminates [45]. This along with the temperature dependent friction condition at the tool-workpiece interface suggests that both pressure and coefficient of friction are sensitive to changes in temperature and analyzing the temperatures at the cutting interface during drilling can aid in predicting the thrust force and torque generation at any point in time including the hole exit which will enable the optimization of process parameters to ensure efficient drilling and obtain quality holes without damage.

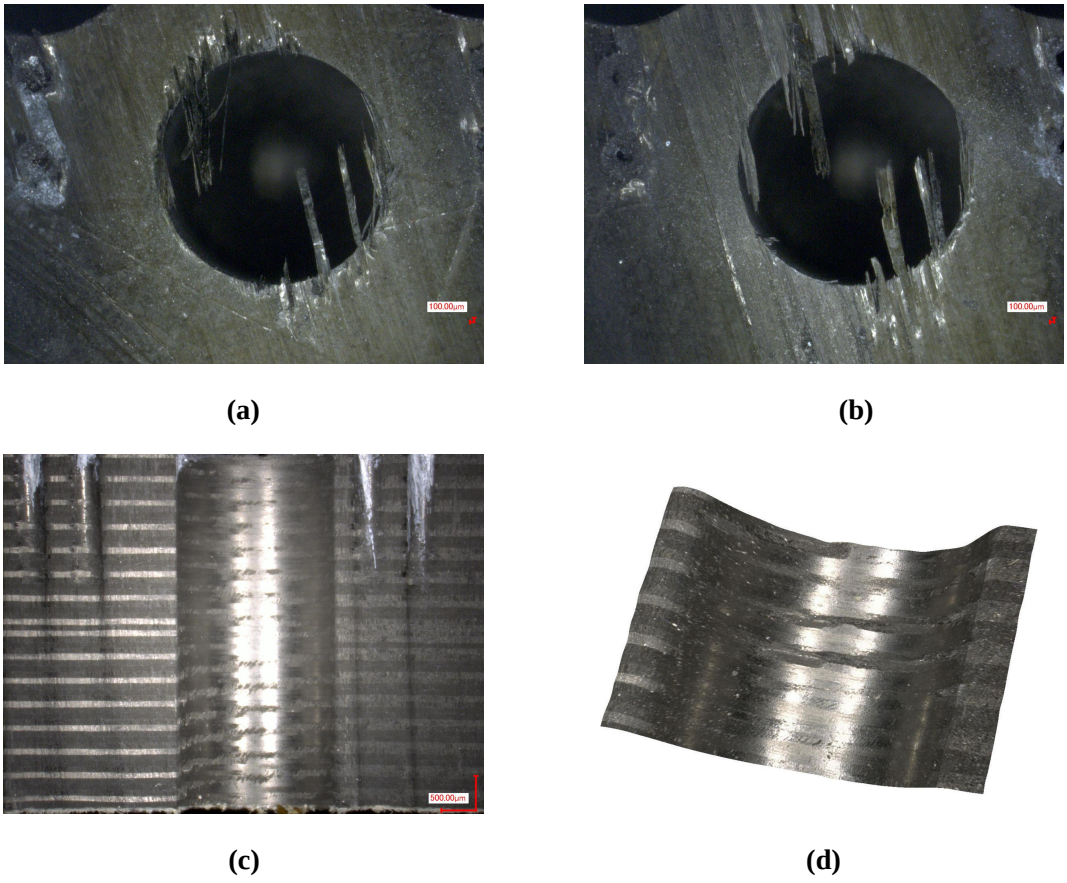

Figure 6.19: Surface and exit of drilled holes in CFRP laminate: a) Hole exit for drilling at 0.04 mm/rev feed and 4000 RPM rotational speed. (b) Hole exit for drilling at 0.05 mm/rev feed and 4000 RPM rotational speed. (c) Cross-section view of hole wall. (d) Hole wall surface

The exit of the drilled holes was observed using the Keyence VH-X100 microscope. The exits for larger feeds show signs of smearing, burrs, and protrusions which can be attributed to the higher cutting forces at the hole exit during drilling as can be seen in Figure 6.19(a) and (b). The holes were bisected using a water jet and the surface of the holes was investigated as exhibited in Figure 6.19 (c) and (d). The surfaces were in good condition and showed no significant sign of damage apart from scratches in the middle region. No major wear was observed on the PCD drill due to its excellent wear resistance even after repeated usage which could be assigned as a probable reason for no observable damage on the surface of the holes. Also, for a couple of the drilling configurations, the temperature on the hole wall surface was estimated to be relatively high compared to the glass transition temperature (T_g) which could have resulted in damages such as burning, delamination or surface cavities [83, 84]. However, due to larger feeds, the drilling times are proportionately short, resulting in very little contact time between the tool and the workpiece surface leading to no substantial damage incurred.

Chapter 7

Conclusion

This study proposes a predictive drilling model that incorporates mechanical stresses on the drill tip with the finite element temperature models of both the tool and the workpiece to estimate the thrust force and torque generation during drilling for different drilling configurations. The drill margin region and a temperature-dependent tribological property coefficient of friction are introduced into the drilling model to improve torque predictions. The drilling operations are simulated by a moving heat source based on the geometry of the tool and workpiece which estimates the temperature distributions to the drill and CFRP in the form of heat partition. The results suggest that around 25-35% of the total heat is carried away in the form of chips while the rest is transferred to the tool and workpiece. The heat transferred into the workpiece decreases noticeably with increasing feed at the same rotational speed. Less heat is directed toward the workpiece with an increase in rotating speed, and more heat is transferred in the direction of the material with a decrease in speed.

The thrust force and torque predictions at characteristic time points agree with the experimental force measurements. Increasing the feed and rotational speed causes contact conditions at the tool-workpiece junction to change. The material properties of CFRP laminate change due to the temperature rise. This causes an increase in contact area at the tool-workpiece interface during the running-in

stage, which decreases the pressure along the cutting edge, while on the contrary, the tangential stress increases along the main cutting edge because of the shearing and removal of material during machining. Larger feeds cause the chip area to increase and the specific cutting energy to decrease, resulting in lower maximum pressure and tangential stress on the main cutting edge while the cutting forces increase. On the contrary, higher rotational speeds cause the specific energy to increase and in turn, increase the maximum pressure and tangential stresses while the cutting forces decrease. The maximum pressure on the drill margin region however increases with a rise in both feed and rotational speed. High pressure can result in chip accumulation on the drill margin causing changes in the contact conditions leading to abrupt rise in thrust force and torque yielding inefficient drilling. Significant chip accumulation on the cutting edge is observed in the case of higher feeds (0.05 mm/rev) and slower rotational speeds (3000 RPM) causing a substantial discrepancy between the prediction and experimental results during the stable stage of drilling.

The effects of temperature rise on the CFRP are also evident during the stable stage of drilling as the peak pressure on the drill margin faces a decline because the workpiece material softens beyond the glass transition temperature (T_g), making it easier to cut, which prompts the thrust force and torque values to drop as well. The heat partition results are utilized to predict the hole wall surface temperature during the drilling operation. The variation of maximum pressure and coefficient of friction at the drill-margin workpiece interface as a function of temperature is similar to the storage modulus and loss modulus profiles obtained from the dynamic mechanical analysis (DMA) of CFRP laminates and therefore can be used to predict the thrust force and torque values at any instance during drilling allowing better control over the process parameters and surface quality. The hole exit and surface of the CFRP laminates were also investigated. Although burrs and scratches were present at the hole exit at larger feeds owing to higher cutting forces, no significant damage was observed on the hole surface till the exit. This was attributed to the wear resistance of the PCD drill even after continuous usage and a relatively short contact time at the interface despite surface temperature estimations from the FE analysis going well over the glass transition temperature

(T_g) of CFRP.

As part of future endeavors, the thrust force and torque values will be approximated at every instance of the total drill time using the proposed drilling model instead of just the characteristic time points to accurately predict the conditions at the cutting zone during drilling operations. Also, more abusive cases of drilling experiments accompanied by drilling with a worn-out tool will be conducted to better understand the integrity of the hole surface of CFRP laminate during dry drilling.

Bibliography

[1] Ross, C. T. (2005). A conceptual design of an underwater missile launcher. Ocean Engineering, 32(1), 85-99.

[2] Soutis, C. (2005). Fibre reinforced composites in aircraft construction. Progress in aerospace sciences, 41(2), 143-151.

[3] Ravishankar, B., Nayak, S. K., & Kader, M. A. (2019). Hybrid composites for automotive applications–A review. Journal of Reinforced Plastics and Composites, 38(18), 835-845.

[4] Ullah, H., Harland, A. R., & Silberschmidt, V. V. (2015). Dynamic bending behaviour of woven composites for sports products: Experiments and damage analysis. Materials & Design, 88, 149-156.

[5] Ashby, M. F. (1997). Material property charts. In Materials Selection and Design (pp. 266-280). ASM international.

[6] Rubino, F., Nisticò, A., Tucci, F., & Carlone, P. (2020). Marine application of fiber reinforced composites: a review. Journal of Marine Science and Engineering, 8(1), 26.

[7] Teti, R. (2002). Machining of composite materials. CIRP Annals, 51(2), 611-634.

[8] Melentiev, R., Priarone, P. C., Robiglio, M., and Settineri, L. (2016). Effects of tool geometry and process parameters on delamination in CFRP drilling: An overview. Procedia Cirp, 45, 31-34.

[9] Xu, J., Geier, N., Shen, J., Krishnaraj, V., and Samsudeensadham, S. (2023). A review on CFRP drilling: fundamental mechanisms, damage issues, and approaches toward high-quality drilling. Journal of Materials Research and Technology.

[10] Isbilir, O., & Ghassemieh, E. (2013). Numerical investigation of the effects of drill geometry on drilling induced delamination of carbon fiber reinforced composites. Composite Structures, 105, 126-133.

[11] Xu, J., & El Mansori, M. (2017). Wear characteristics of polycrystalline diamond tools in orthogonal cutting of CFRP/Ti stacks. Wear, 376, 91-106.

[12] https://www.drillbitwarehouse.com/exploring-the-different-types-of-twist-drill-point-angles/

[13] Wan, M., Li, S. E., Yuan, H., & Zhang, W. H. (2019). Cutting force modelling in machining of fiber-reinforced polymer matrix composites (PMCs): a review. Composites Part A: Applied Science and Manufacturing, 117, 34-55.

[14] Hintze, W., Clausen, R., Schütte, C., & Kroll, K. (2018). Evaluation of the total cutting force in drilling of CFRP: a novel experimental method for the analysis of the cutting mechanism. Production engineering, 12, 431-440.

[15] Bhattacharyya, D., & Horrigan, D. P. W. (1998). A study of hole drilling in Kevlar composites. Composites science and technology, 58(2), 267-283.

[16] Zhang, L. C., Zhang, H. J., & Wang, X. M. (2001). A force prediction model for cutting unidirectional fibre-reinforced plastics.

[17] Gultekin, M. S., Isik, B., & Jun, M. B. G. (2024). A New Methodology for Drilling of Carbonfiber Reinforced Polymer Composite (CFRP) Material. International Journal of Precision Engineering and Manufacturing, 1-12.

[18] Wang, D., Jiao, F., & Mao, X. (2020). Mechanics of thrust force on chisel edge in carbon fiber reinforced polymer (CFRP) drilling based on bending failure theory. International Journal of Mechanical Sciences, 169, 105336.

[19] Dowling, N. E., Kampe, S. L., & Kral, M. V. (1999). Mechanical behavior of materials: engineering methods for deformation, fracture, and fatigue.

[20] Xu, J., An, Q., Cai, X., & Chen, M. (2013). Drilling machinability evaluation on new developed high-strength T800S/250F CFRP laminates. International Journal of Precision Engineering and Manufacturing, 14, 1687-1696.

[21] Chandrasekharan, V. (1996). A model to predict the three-dimensional cutting force system for drilling with arbitrary point geometry. University of Illinois at Urbana-Champaign.

[22] Xiao, J., Gao, N., Wang, G., Huang, P., & He, J. (2024). Force coefficient characterization in machining of UD-CFRP using numerical-analytical approach. Polymers and Polymer Composites, 32, 09673911241248420..

[23] Voss, R., Seeholzer, L., Kuster, F., & Wegener, K. (2019). Analytical force model for orthogonal machining of unidirectional carbon fibre reinforced polymers (CFRP) as a function of the fibre orientation. Journal of Materials Processing Technology, 263, 440-469.

[24] Qi, Z., Zhang, K., Cheng, H., Wang, D., & Meng, Q. (2015). Microscopic mechanism based force prediction in orthogonal cutting of unidirectional CFRP. The International Journal of Advanced Manufacturing Technology, 79, 1209-1219.

[25] Yan, X., Zhang, K., Cheng, H., Luo, B., & Hou, G. (2019). Force coefficient prediction for drilling of UD-CFRP based on FEM simulation of orthogonal cutting. The International Journal of Advanced Manufacturing Technology, 104, 3695-3716.

[26] Zou, G. P., Yellowley, I., & Seethaler, R. J. (2009). A new approach to the modeling of oblique cutting processes. International Journal of Machine Tools and Manufacture, 49(9), 701-707.

[27] Jia, Z. Y., Zhang, C., Wang, F. J., & Fu, R. (2020). A mechanistic prediction model for thrust force and torque during drilling of CFRP/Ti stacks. The International Journal of Advanced Manufacturing Technology, 106, 3105-3115. Zou, G. P., Yellowley, I., & Seethaler, R. J. (2009). A new approach to the modeling of oblique cutting processes. International Journal of Machine Tools and Manufacture, 49(9), 701-707.

[28] Song, G., Sui, S., & Tang, L. (2015). Precision prediction of cutting force in oblique cutting operation. The International Journal of Advanced Manufacturing Technology, 81(1), 553-562.

[29] Melentiev, R., Priarone, P. C., Robiglio, M., & Settineri, L. (2016). Effects of tool geometry and process parameters on delamination in CFRP drilling: An overview. Procedia Cirp, 45, 31-34.

[30] Hocheng, H., & Tsao, C. C. (2006). Effects of special drill bits on drilling-induced delamination of composite materials. International Journal of Machine Tools and Manufacture, 46(12-13), 1403-1416.

[31] Karpat, Y., Bahtiyar, O., Değer, B., & Kaftanoğlu, B. (2014). A mechanistic approach to investigate drilling of UD-CFRP laminates with PCD drills. CIRP Annals, 63(1), 81-84.

[32] Pan, Z., Wang, L., Fang, Q., Sun, Z., & Qu, W. (2022). Study on tool deflection compensation method based on cutting force observer for orbital drilling of CFRP/Ti stacks. Journal of Manufacturing Processes, 75, 450-460.

[33] Wang, C. Y., Chen, Y. H., An, Q. L., Cai, X. J., Ming, W. W., & Chen, M. (2015). Drilling temperature and hole quality in drilling of CFRP/aluminum stacks using diamond coated drill. International Journal of Precision Engineering and Manufacturing, 16, 1689-1697.

[34] DiBenedetto, A. T. (1987). Prediction of the glass transition temperature of polymers: a model based on the principle of corresponding states. Journal of Polymer Science Part B: Polymer Physics, 25(9), 1949-1969.

[35] Brydson, J. A. (1999). Plastics materials. Elsevier.

[36] Khashaba, U. A., & El-Keran, A. A. (2017). Drilling analysis of thin woven glass-fiber reinforced epoxy composites. Journal of Materials Processing Technology, 249, 415-425.

[37] Wang, H., Zhang, X., & Duan, Y. (2018). Effects of drilling area temperature on drilling of carbon fiber reinforced polymer composites due to temperature-dependent properties. The International Journal of Advanced Manufacturing Technology, 96, 2943-2951.

[38] Liang, X., & Wu, D. (2019). Tribological properties of carbon-fibre-reinforced plastic against tungsten carbide under dry condition. Tribology International, 134, 118-128.

[39] Tang, W., Chen, Y., Yang, H., Wang, H., & Yao, Q. (2018). Numerical investigation of delamination in drilling of carbon fiber reinforced polymer composites. Applied Composite Materials, 25, 1419-1439.

[40] Feito, N., Diaz-Álvarez, J., López-Puente, J., & Miguelez, M. H. (2016). Numerical analysis of the influence of tool wear and special cutting geometry when drilling woven CFRPs. Composite Structures, 138, 285-294.

[41] Wang, F., Wang, X., Zhao, X., Bi, G., & Fu, R. (2020). A numerical approach to analyze the burrs generated in the drilling of carbon fiber reinforced polymers (CFRPs). The International Journal of Advanced Manufacturing Technology, 106, 3533-3546.

[42] Chen, C., Zhao, Q., Wang, A., Shi, Z., & Bai, Y. (2024). Numerical study on the heat effect on the drilling damage of Ti/CFRP stacks. Polymer Composites.

[43] Sheikh-Ahmad, J. Y., Almaskari, F., Hafeez, F., & Meng, F. (2019). Evaluation of heat partition in machining CFRP using inverse method. Machining Science and Technology.

[44] Yashiro, T., Ogawa, T., & Sasahara, H. (2013). Temperature measurement of cutting tool and machined surface layer in milling of CFRP. International Journal of Machine Tools and Manufacture, 70, 63-69.

[45] Karpat, Y., Karagüzel, U., & Bahtiyar, O. (2020). A thermo-mechanical model of drill margin-borehole surface interface contact conditions in dry drilling of thick CFRP laminates. International Journal of Machine Tools and Manufacture, 154, 103565.

[46] Zitoune, R., Krishnaraj, V., Collombet, F., & Le Roux, S. (2016). Experimental and numerical analysis on drilling of carbon fibre reinforced plastic and aluminium stacks. Composite Structures, 146, 148-158.

[47] Bono, M., & Ni, J. (2002). A model for predicting the heat flow into the workpiece in dry drilling. J. Manuf. Sci. Eng., 124(4), 773-777.

[48] Sadek, A., Shi, B., Meshreki, M., Duquesne, J., & Attia, M. H. (2015). Prediction and control of drilling-induced damage in fibre-reinforced polymers using a new hybrid force and temperature modelling approach. CIRP Annals, 64(1), 89-92.

[49] Santiuste, C., Díaz-Álvarez, J., Soldani, X., & Miguélez, H. (2014). Modelling thermal effects in machining of carbon fiber reinforced polymer composites. Journal of reinforced plastics and composites, 33(8), 758-766.

[50] Lazoglu, I., Poulachon, G., Ramirez, C., Akmal, M., Marcon, B., Rossi, F., ... & Krebs, M. (2017). Thermal analysis in Ti-6Al-4V drilling. CIRP Annals, 66(1), 105-108.

[51] Kuo, C. L., Soo, S. L., Aspinwall, D. K., Thomas, W., Carr, C., Pearson, D., ... & Leahy, W. (2015, March). Performance of multi-margin coated tools in one-shot drilling of metallic-composite stack materials under varying feed rate and pecking conditions. In International MATADOR Conference (pp. 295-312). Cham: Springer International Publishing.

[52] Bonnet, C., Poulachon, G., Rech, J., Girard, Y., & Costes, J. P. (2015). CFRP drilling: Fundamental study of local feed force and consequences on hole exit damage. International Journal of Machine Tools and Manufacture, 94, 57-64.

[53] Fu, R., Jia, Z., Wang, F., Jin, Y., Sun, D., Yang, L., & Cheng, D. (2018). Drill-exit temperature characteristics in drilling of UD and MD CFRP composites based on infrared thermography. International Journal of Machine Tools and Manufacture, 135, 24-37.

[54] Shu, L., Li, S., Fang, Z., Kizaki, T., Kimura, K., Arai, G., ... & Sugita, N. (2021). Study on dedicated drill bit design for carbon fiber reinforced polymer drilling with improved cutting mechanism. Composites Part A: Applied Science and Manufacturing, 142, 106259.

[55] Bahadur, S. (1970). The correlation of frictional and viscoelastic properties of polymers. University of Michigan.

[56] Kaya, I., & Parlar, Z. (2020). The investigation of tribological behavior of carbon fiber-reinforced composite materials. Industrial Lubrication and Tribology, 72(2), 211-216.

[57] Bora, M. O., Coban, O. N. U. R., Sinmazcelik, T., & Gunay, V. (2010). Effect of fiber orientation on scratch resistance in unidirectional carbon-fiber-reinforced polymer matrix composites. Journal of reinforced plastics and composites, 29(10), 1476-1490.

[58] Mohee, F. M., Al-Mayah, A., & Plumtree, A. (2016). Friction characteristics of CFRP plates in contact with copper plates under high contact pressure. Journal of Composites for Construction, 20(5), 04016022.

[59] Afrasiabi, M., Klippel, H., Röthlin, M., & Wegener, K. (2021). Parameter identification of a friction model in metal cutting simulations with gpu-accelerated meshfree methods. WCCM-ECCOMAS2020.

[60] Černe, B., Bergant, Z., Šturm, R., Tavčar, J., & Zorko, D. (2022). Experimental and numerical analysis of laminated carbon fibre-reinforced polymer gears with implicit model for coefficient-of-friction evaluation. Journal of Computational Design and Engineering, 9(1), 246-262.

[61] Xu, J., Deng, Y., Wang, C., & Liang, G. (2021). Numerical model of unidirectional CFRP in machining: Development of an amended friction model. Composite Structures, 256, 113075.

[62] Wang, D., Jiao, F., & Mao, X. (2020). Mechanics of thrust force on chisel edge in carbon fiber reinforced polymer (CFRP) drilling based on bending failure theory. International Journal of Mechanical Sciences, 169, 105336.

[63] Liu, S., Yang, T., Liu, C., Jin, Y., Sun, D., & Shen, Y. (2020). Mechanistic force modelling in drilling of AFRP composite considering the chisel edge extrusion. The International Journal of Advanced Manufacturing Technology, 109, 33-44.

[64] Gaikhe, V., Gaikhe, Y. S., & Patil, J. P. (2018). Prediction of thrust force and torque in drilling of glass fiber reinforced plastic using mechanistic force model approach. Procedia CIRP, 77, 187-190.

[65] Lazar, M. B., & Xirouchakis, P. (2013). Mechanical load distribution along the main cutting edges in drilling. Journal of Materials Processing Technology, 213(2), 245-260.

[66] Altintas, Y. (2012). Manufacturing automation: metal cutting mechanics, machine tool vibrations, and CNC design. Cambridge university press.

[67] Ackroyd, B., Akcan, N. S., Chhabra, P., Krishnamurthy, K., Madhavan, V., Chandrasekar, S., ... & Farris, T. N. (2001). Exploration of contact conditions in machining. Proceedings of the Institution of Mechanical Engineers, Part B: Journal of Engineering Manufacture, 215(4), 493-507.

[68] Grzesik, W., & Rech, J. (2019). Development of tribo-testers for predicting metal cutting friction. Journal of Machine Engineering, 19.

[69] Joven, R., Das, R., Ahmed, A., Roozbehjavan, P., & Minaie, B. (2012, October). Thermal properties of carbon fiber-epoxy composites with different fabric weaves. In SAMPE international symposium proceedings (Vol. 14). Charleston USA.

[70] Macias, J. D., Bante-Guerra, J., Cervantes-Alvarez, F., Rodrìguez-Gattorno, G., Arés-Muzio, O., Romero-Paredes, H., ... & Alvarado-Gil, J. J. (2019). Thermal characterization of carbon fiber-reinforced carbon composites. Applied Composite Materials, 26, 321-337.

[71] Zhou, Y., Ramaneti, R., Anaya, J., Korneychuk, S., Derluyn, J., Sun, H., ... & Kuball, M. (2017). Thermal characterization of polycrystalline diamond thin film heat spreaders grown on GaN HEMTs. Applied Physics Letters, 111(4).

[72] Cao, P. L., Liu, B. C., Yin, K., & Zhang, Z. P. (2006). Optimization design and residual thermal stress analysis of PDC functionally graded materials. Journal of Zhejiang University-Science A, 7, 1318-1323.

[73] Zohdi, N., & Yang, R. (2021). Material anisotropy in additively manufactured polymers and polymer composites: a review. Polymers, 13(19), 3368.

[74] Medeiros, J. C., & Filho, J. M. C. (2020). A comparison of different heat flux density distribution models to predict the temperature in the drilling process. The International Journal of Advanced Manufacturing Technology, 109, 1997-2008.

[75] Watts, R. G. (1969). Temperature distributions in solid and hollow cylinders due to a moving circumferential ring heat source.

[76] Shi, B., Sadek, A., Meshreki, M., Attia, H., & Duquesne, J. (2017). Numerical and experimental investigation of thermal damage in drilling of CFRP composites. Int. J. Robot. Mechatron, 4, 16-21.

[77] Segurajauregui, U., & Arrazola, P. J. (2015). Heat-flow determination through inverse identification in drilling of aluminium workpieces with MQL. Production Engineering, 9, 517-526.

[78] Senis, E. C., Golosnoy, I. O., Dulieu-Barton, J. M., & Thomsen, O. T. (2019). Enhancement of the electrical and thermal properties of unidirectional carbon fibre/epoxy laminates through the addition of graphene oxide. Journal of Materials Science, 54(12), 8955-8970.

[79] Melkote, S. N., & Subbiah, S. (2013). Size effects in machining tribology. Encyclopedia of Tribology, Springer, 3108-3114.

[80] Niketh, S., & Samuel, G. L. (2021). Surface textured drill tools—An effective approach for minimizing chip evacuation force and burr formation during high aspect ratio machining of titanium alloy. Journal of Manufacturing Science and Engineering, 143(4), 041005.

[81] Shard, A., Garg, M. P., Gupta, V. (2023). Experimental investigation and statistical modelling of cutting force and torque during rotary ultrasonic drilling of polyetherimide composite. Strength of Materials, 55(2), 355-370.

[82] Ning, F. D., Cong, W. L., Pei, Z. J., Treadwell, C. (2016). Rotary ultrasonic machining of CFRP: a comparison with grinding. Ultrasonics, 66, 125-132.

[83] Girot, F., Dau, F., Gutiérrez-Orrantia, M. E. (2017). New analytical model for delamination of CFRP during drilling. Journal of Materials Processing Technology, 240, 332-343.

[84] Henerichs, M., Voss, R., Kuster, F., Wegener, K. (2015). Machining of carbon fiber reinforced plastics: Influence of tool geometry and fiber orientation on the machining forces. CIRP Journal of Manufacturing Science and Technology, 9, 136-145.

Appendix A

Drill Geometry

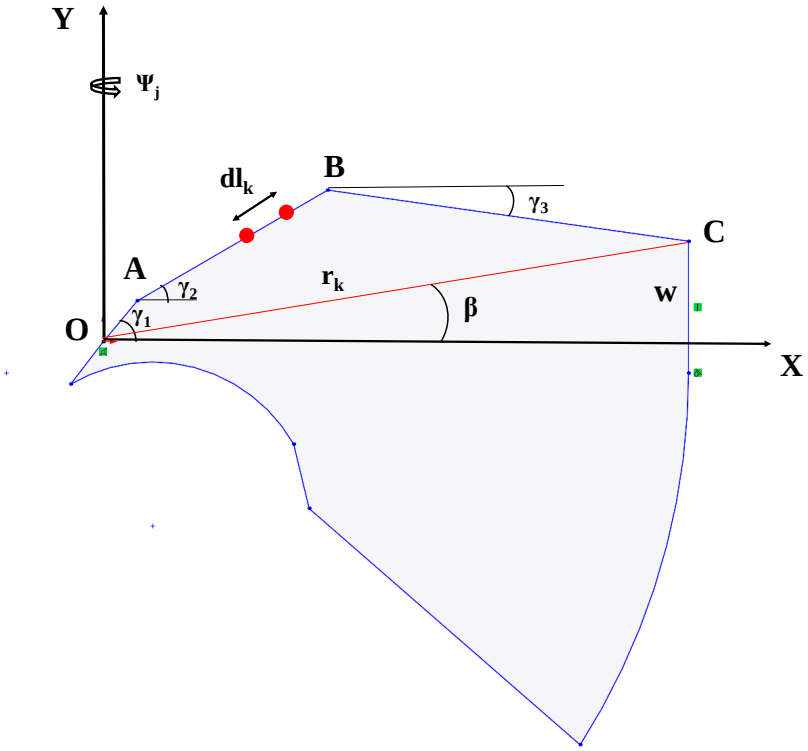

Figure A.1: Schematics of the cutting edge of PCD double tip angle drill

Figure A.1 shows the front view schematics of the drill tip geometry. The chisel edge region OA has a length of 532 μm and is inclined at an angle of $\gamma_1 = 50°$ from the axis of the drill. Similarly, the main cutting edge is composed of two sections: the primary cutting edge AB (L_{AB}=950 μm, $\gamma_2 = 35°$) and the secondary cutting edge BC (L_{BC}=950 μm, $\gamma_3 = 5°$). The drill margin region CD is demonstrated in Figure X. Successive points termed k are assigned on the whole drill tip. Each incremental rotation (Ψ_j) of the drill is termed j. The distance between two consecutive points is considered the incremental elemental length dl for calculating the unit thrust force and torque, as discussed in Chapter 4. The vertical height of the drill tip for every unit element can be measured using Equation A.1.

$$z = \frac{H_{OC}}{k} \tag{A.1}$$

The drilling time t_{drill} can be obtained by dividing the thickness of the laminate (L) by the feed rate (f_r).

The equations illustrated in Table A.1 can be used to determine the three-dimensional location of any point along the drill edge (from O to C) depending on drill angles.

Table A.1: Location calculation for points on drill tip

Chisel Edge (OA)	**Primary Cutting Edge (AB)**	**Secondary Drilling Edge (BC)**	**Drill Margin (CD)**
$x_k = r_{ch}\cos\gamma_1$	$x_k = (z_{k-1} - z_k)\tan(\theta_1) + x_{k-1}$	$x_k = (z_{k-1} - z_k)\tan(\theta_2) + x_{k-1}$	$x_k = x_{k-1}$
$y_k = r_{ch}\sin\gamma_1$	$y_k = (z_{k-1} - z_k)\tan(\theta_2)\tan(\gamma_2) + y_{k-1}$	$y_k = y_{k-1} - (z_{k-1} - z_k)\tan(\theta_2)\tan(\gamma_3)$	$y_k = y_{k-1}$
$z_k = z_k$	$z_k = z_k$	$z_k = z_k$	$z_k = z_k$
$\beta_k = 50°$	$\beta_k = \tan^{-1}(y/x)$	$\beta_k = \tan^{-1}(y/x)$	$\beta_k = \tan^{-1}(y/x)$

The course of any point (x_k, y_k, z_k) of the tip of the drill can be computed at any time interval by the following Equations adapted from literature [45]:

$$x_{k,j} = r_k \cos(\beta_k + \Psi_j) \tag{A.2}$$

$$y_{k,j} = r_k \sin(\beta_k + \Psi_j) \tag{A.3}$$

$$z_{k,j} = (\frac{L + H_{OC}}{\Delta\Psi}) \times j \tag{A.4}$$

Entry and exit zones can be determined as a function of time by analyzing whether any point on the drill tip is inside the workpiece.

We have adapted the formulations proposed by Lazar et al. [65] to calculate the angles on the cutting edge of the drill in Chapter 4.

The point angle is the angle between the cutting edge and the axis of the drill. The double-point angle drill has two individual angles for the two stages of the main cutting edge. The measurements taken with the digital microscope are shown in Equation A.5.

$$\theta(r) = \begin{cases} 67.5^\circ & \text{if } 0 < r \leq r_{AB} \\ 45^\circ & \text{if } r_{AB} < r \leq r_{BC} \end{cases} \tag{A.5}$$

Here, r_{AB} is the radius of the primary cutting edge region AB, r_{BC} is the secondary cutting edge region BC, r_{CD} is the drill margin region CD, and θ is the point angle.

The web angle is the angle between any point on the cutting edge and the projection of the cutting edge up until that point on the plane perpendicular to the axis of the drill. The Equation A.6 can be used to calculate the web angle.

$$\beta(r) = \begin{cases} 50^\circ & \text{if } 0 < r \leq r_{OA} \\ \arctan\left(\frac{y(i)}{x(i)}\right) & \text{if } r_{OA} < r \leq r_{BC} \end{cases} \tag{A.6}$$

Here, β is the web angle, x is the projection on the perpendicular plane, y is the point on the cutting edge, and w is the web thickness.

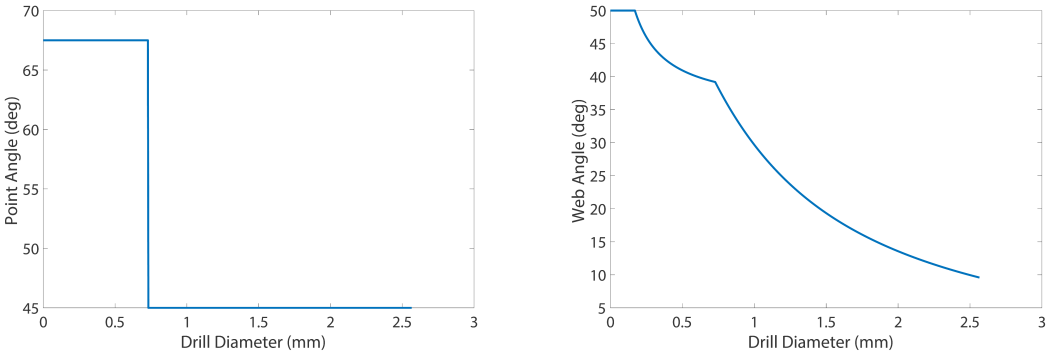

Figure A.2: Angle measurements: (a) Point angle. (b) Web angle.

The cutting angle is calculated by equation A.7.

$$p(r) = \begin{cases} \arctan\left(\frac{f}{2\pi r}\right) & \text{if } 0 < r \leq r_{BC} \end{cases} \tag{A.7}$$

Here, f is the feed, r is the drill radius, and p is the cutting angle.

The inclination angle can be calculated with Equation A.8.

$$i(r) = \begin{cases} \arcsin\left(\sin(\beta)\cos(p)\sin(\theta) + \sin(p)\cos(\theta)\right) & \text{if } 0 < r \leq r_{BC} \end{cases} \tag{A.8}$$

The orientation of the angle on the rake face of the cutting edge is called the normal rake angle. The normal rake angle on the cutting edge can be calculated using Equation AA.9.

$$\alpha_n(r) = \arctan\left(\frac{\tan(\theta_l)\cos(\beta)}{\sin(\theta) - \cos(\theta)\tan(\theta_l)\sin(\beta)}\right) - \arctan\left(\frac{\sin(\beta)\cos(\theta) - \sin(\theta)\tan(p)}{\cos(\beta)}\right) \tag{A.9}$$

θ_l is the local helix angle which can be calculated using Equation A.10.

$$\theta_l(r) = \tan^{-1}\left(\tan(H) \times \frac{r}{R}\right) \tag{A.10}$$

H is the reference helix angle measured at 25° and R is the radius of the drill.

Since the chisel edge has an angle concerning the axis of the drill the inclination angle on the chisel edge region is not zero as seen in Figure A.1. As a result the chisel edge section also has a static rake angle which can be calculated by Equation A.11.

$$\alpha_s(r) = \arctan\left(\frac{\tan(\theta)\sin(\psi)\sin(\theta)}{\sin(\theta) + \tan(\theta)\cos(\theta)\cos(\psi)}\right) \tag{A.11}$$

Here, θ is the point angle of the primary cutting edge, and ψ is the chisel edge angle measured to be 125°.

The chip flow angle has been assumed to be equal to the inclination angle, i.

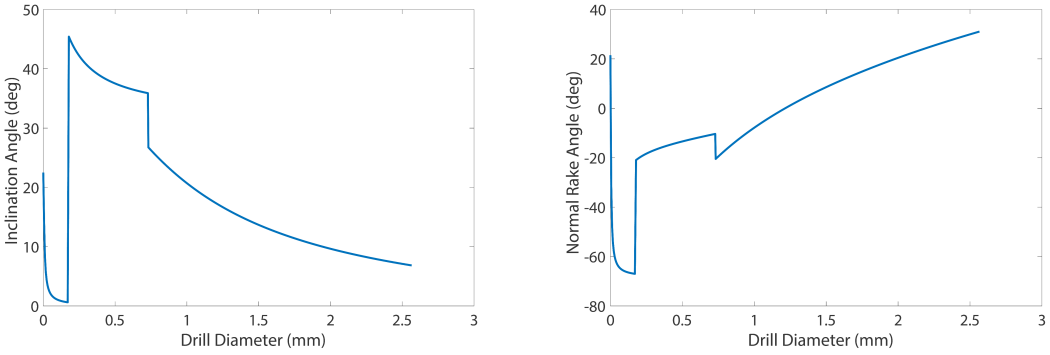

Figure A.3: Angle measurements: (a) Inclination angle. (b) Normal rake angle.

Indentation tests were performed to analyze the effect of chisel edge geometry on the extrusion force generated during the drilling of CFRP laminates. The drill was used to indent the thick CFRP laminate and the force data was measured for indentation depths of 10 and 15 μm. The force vs displacement plots shown in Figure A.4 suggested that with an increase in indentation depth, the force increased suggesting higher extrusion forces being generated by the chisel edge at larger feeds during drilling.

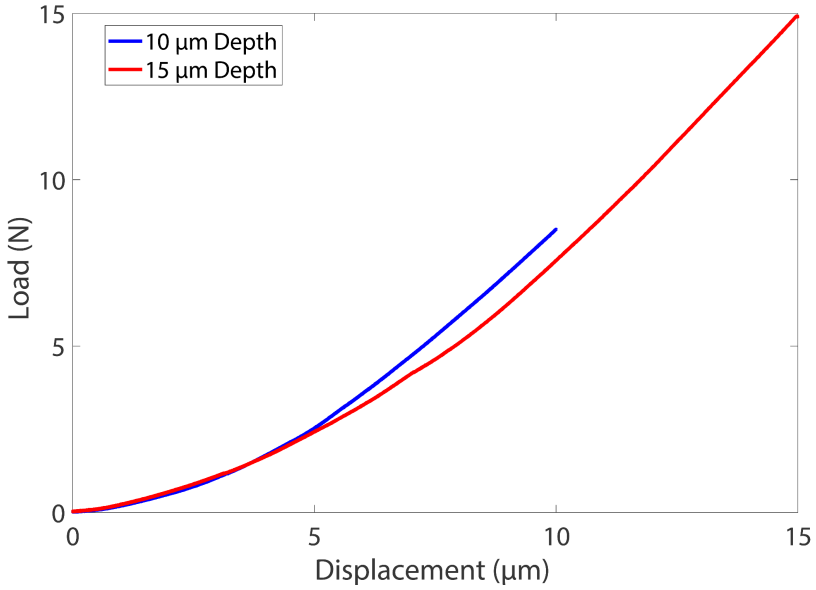

Figure A.4: Indentation test of CFRP laminate using the chisel edge of the PCD drill.